

Empirical limb-darkening coefficients & transit parameters of known exoplanets from *TESS*

JAYSHIL A. PATEL ¹ AND NÉSTOR ESPINOZA ^{2,3}

¹*Department of Astronomy, Stockholm University, AlbaNova University Center, 10691 Stockholm, Sweden*

²*Space Telescope Science Institute, 3700 San Martin Drive, Baltimore, MD 21218, USA*

³*Department of Physics & Astronomy, Johns Hopkins University, Baltimore, MD 21218, USA*

(Received; Revised)

Submitted to AJ

ABSTRACT

Although the main goal of the Transiting Exoplanet Survey Satellite (*TESS*) is to search for new transiting exoplanets, its data can also be used to study in further detail already known systems. The *TESS* bandpass is particularly interesting to study the limb-darkening effect of the stellar host which is imprinted in transit lightcurves, as the widely used PHOENIX and ATLAS stellar models predict different limb-darkening profiles. Here we study this effect by fitting the transit lightcurves of 176 known exoplanetary systems observed by *TESS*, which allows us to extract empirical limb-darkening coefficients (LDCs) for the widely used quadratic law, but also updated transit parameters (including ephemerides refinements) as a byproduct. Comparing our empirically obtained LDCs with theoretical predictions, we find significant offsets when using tabulated *TESS* LDCs. Specifically, the u_2 coefficients obtained using PHOENIX models show the largest discrepancies depending on the method used to derive them, with offsets that can reach up to $\Delta u_2 \approx 0.2$ on average. Most of those average offsets disappear, however, if one uses the SPAM algorithm introduced by Howarth (2011) to calculate the LDCs instead. Our results suggest, however, that for stars cooler than about 5000 K, no methodology is good enough to explain the limb-darkening effect: we observe a sharp deviation between measured and predicted LDCs on both quadratic LDCs of order $\Delta u_1, \Delta u_2 \approx 0.2$ for those cool stars. We recommend caution when assuming limb-darkening coefficients as perfectly known thus, in particular for these cooler stars when analyzing *TESS* transit lightcurves.

Keywords: editorials, notices — miscellaneous — catalogs — surveys

1. INTRODUCTION

The phenomenon of limb-darkening on stars — the observed intensity decrease towards their limb — has for long been recognized as a natural consequence of temperature gradients in stellar atmospheres (Schwarzschild 1906). Although a complex effect in nature, parametric formulations of it have been shown to be very practical to use when the effect needs to be modelled. These so-called “limb-darkening laws” have been mainly motivated from an observational perspective and have been formulated with certain use-cases in mind (see, for example Claret 2000; Diaz-Cordoves & Gimenez 1992; Sing

et al. 2009; KlingleSmith & Sobieski 1970; Claret & Hauschildt 2003). In exoplanetary science, in particular, the most popular laws to date are the linear law (Schwarzschild 1906), the quadratic law (Kopal 1950) and the non-linear law (Claret 2000). Their functional forms are,

$$\frac{I(\mu)}{I(1)} = 1 - a(1 - \mu); \text{ (the linear law),}$$

$$\frac{I(\mu)}{I(1)} = 1 - u_1(1 - \mu) - u_2(1 - \mu)^2; \text{ (the quadratic law),}$$

$$\frac{I(\mu)}{I(1)} = 1 - \sum_{n=1}^4 c_n(1 - \mu^{n/2}); \text{ (the non-linear law).}$$

Here a , (u_1, u_2) and (c_1, c_2, c_3, c_4) are the so-called limb darkening coefficients (LDCs) of these respective

laws and μ represents the cosine of the angle θ - the angle between the line of sight and the normal to the surface. The reason for the popularity of these laws is most likely related with the fact that these give rise to very fast lightcurve computations (Mandel & Agol 2002), which in turn makes them the most practical to use. Among them, the quadratic law is by far the most widely used in the exoplanet literature mainly due to the fact that it gives rise to fast and efficient computation of lightcurves in some of the most popular lightcurve computing methods/algorithms (e.g., `batman`; Kreidberg 2015). The simplicity of this law also makes it an attractive one to use for researchers: it is defined by only two parameters which can even be fitted along with the rest of the other transit parameters if stellar model atmospheres are suspected to not be appropriate for a given use-case. While it might not always be the most accurate law to use (see, e.g., Southworth 2008; Hayek et al. 2012; Espinoza & Jordán 2016), its usage is nonetheless widespread across transiting exoplanet studies because of the aforementioned reasons.

The details of the limb-darkening effect become important when one wants to fit an exoplanet transit lightcurve because its shape is strongly modulated by the effect (Mandel & Agol 2002; Seager & Mallén-Ornelas 2003). Incorrect assumptions about the effect, thus, have the potential to lead to biases on the retrieved transit parameters. Indeed, simulations have studied in detail the impact of either fitting or fixing the LDCs (see, e.g., Csizmadia et al. 2013; Espinoza & Jordán 2015; Neilson et al. 2017; Morello et al. 2017) and even the impact the selection of a given limb-darkening law has on the retrieval of the transit parameters (Espinoza & Jordán 2016). Most of these studies conclude that the most conservative assumption is to fit for the coefficients in the transit lightcurve fitting procedure, taking special care on the selection of the limb-darkening law to use for very precise (better than about 200 ppm) transit lightcurves. This suggestion, however, is impractical in cases on which the lightcurve is poorly sampled and/or dominated by systematic noise such as in, e.g., *Hubble Space Telescope* (HST) spectro-photometric measurements (see, e.g., Kreidberg 2018). It is also not clear from the literature how far off empirical LDCs are from stellar model atmospheres predictions, which of all the stellar models available in the literature are the best to use, and which exact method/table one should use if one needed a set of LDCs to either fix or use as priors in the analysis (see, e.g., Hayek et al. 2012; Espinoza & Jordán 2015; Sandford & Kipping 2017). Studies such as that of, e.g., Hayek et al. (2012), Müller et al. (2013a), Espinoza & Jordán (2015) and Macted (2018),

have approached the problem by comparing LDCs empirically determined from transit lightcurves to that of predictions from stellar model atmospheres. This inter-comparison between empirical LDCs and those obtained from actual data are critical not only to inform stellar modellers, but also the community on best practices and uses of stellar model atmospheres for exoplanet transit lightcurves. Such a comparison has the power to aid us in the search for better models, and empirical LDCs could provide good priors especially useful when confronted with low precision lightcurves.

The *Transiting Exoplanet Survey Satellite* (*TESS*; Ricker et al. 2014) mission does not only provide exquisite, almost all-sky photometry with which to look for new transiting exoplanets, but also provides a unique dataset of already *known* exoplanets which is ideal to perform tests on stellar model atmospheres through stellar limb-darkening. Given that most known transiting exoplanetary systems have been thoroughly characterized with ground-based instruments, precise spectroscopic parameters are available for their host stars and thus limb-darkening predictions can be extracted from stellar model atmospheres. The precise photometry being collected by the *TESS* mission, in turn, should allow us to tightly constrain the limb-darkening effect through the LDCs, thus providing a rich dataset to compare against theoretical predictions. Interestingly (and as it will be shown in this work), LDCs from the most widely used stellar model atmospheres to model limb-darkening in exoplanet transit lightcurves, namely, the *ATLAS* (Castelli & Kurucz 2003) and *PHOENIX* (Husser et al. 2013) model atmospheres, have very different values in the *TESS* bandpass depending on which methods one uses to obtain them, which provides a perfect opportunity to test these two stellar model atmospheres (and the methods used to obtain LDCs) against empirical data. In this work, we use recently released *TESS* transit lightcurve data in order to extract limb darkening coefficients for a subset of the known systems observed by the mission in order to perform these tests.

We have organized this work as follows. In Section 2, we describe how we select our targets and download the data for them, along with a description of the modelling procedure used to analyze the lightcurves and to obtain theoretical predictions for our LDCs. We present our findings in Section 3, which are followed by a Discussion in Section 4 and Conclusions and Future Work in Section 5.

2. DATA, SAMPLE SELECTION AND MODELLING

2.1. Selection of targets

Because the main objective of the present work was to characterize the stellar hosts, we chose *TESS* targets that had already known and confirmed transiting exoplanets, and that had precise follow-up observations that allowed for precise stellar (e.g., stellar effective temperatures, gravity, metallicity) and planetary (e.g., via radial-velocity variations) characterization using high-resolution spectroscopy. In addition, only exoplanets observed in 2-minute cadence by *TESS* were selected in order to minimize lightcurve distortions due to the binning of the 30-minute cadence lightcurves (Kipping 2010).

According to the NASA Exoplanet Archive¹, when we started our analysis, more than 4000 exoplanets were known. Among them, we chose transiting exoplanets which were going to be or already were observed by *TESS*. We filtered these planets using the Web TESS Viewing tool (WTV)². At the time of our analysis, the *TESS* mission had observed targets up to sector 32, so we selected targets only up to this sector. There were a total of 1745 of them. Among these systems, we removed from our sample:

- Systems that did not have follow-up high-resolution spectroscopic observations that allowed us to confirm their orbits in an independent way to the transits.
- Multi-planetary systems, which would involve extra complications in the analyses (TTVs, joint fitting of some properties, checks for planet-planet transits).
- Systems that had known physically associated stellar companions, as they could significantly dilute the exoplanet transit lightcurves.

When we analysed these filtered systems, we found that some of them had very low signal-to-noise ratio transit lightcurves. We decided to measure the signal-to-noise ratio of the transits through their transit depths, and decided that systems for which the signal-to-noise ratio of the transit depths were less than 5 would also be removed from our study. After this, a total of 176 targets remained in our sample. Figure 1 shows the range and the distribution of effective temperature (T_{eff}) and surface gravity ($\log(g)$ - in cgs units) of the exoplanet host stars of our target systems. Table 3 shows the values of various stellar properties of each of our host target stars.

2.2. Data and Modelling

We used *juliet* (Espinoza et al. 2019a) to download and fit the 2-minute cadence lightcurve data directly from the Mikulski Archive for Space Telescopes (MAST³) portal in an automated fashion. Times, fluxes and errors were extracted from the PDC-corrected lightcurve products.

The transit lightcurves were modelled within *juliet* using the *batman* (Kreidberg 2015) model. In addition to it, each lightcurve fit also included a Gaussian Process (GP) in order to marginalize either astrophysical or instrumental systematic trends present in the *TESS* lightcurves. In particular, for each lightcurve, we fitted a GP using two kernels: an Exponential-Matèrn kernel and a Quasi-periodic kernel. The first one is a result of multiplying an exponential kernel, which typically samples smooth functions, and a Matèrn 3/2 kernel, which allows to model abrupt changes in the lightcurves, making the resultant multiplied kernel a very flexible one to model instrumental systematics or non-periodic phenomena. The Quasi-periodic kernel we opted to use, on the other hand, was the one introduced in Foreman-Mackey et al. (2017), and of the form,

$$k(x_l, x_m) = \frac{B}{2 + C} e^{-\tau/L} \left[\cos\left(\frac{2\pi\tau}{P_{\text{rot}}}\right) + (1 + C) \right], \quad (1)$$

where B , C , L and P_{rot} are the hyperparameters of the kernel. This is a very useful kernel when it comes to modelling quasi-periodic phenomena such as the one observed in, e.g., starspot rotational modulations. These two kernels are implemented within *juliet* using *celerite* (Foreman-Mackey et al. 2017).

In practice, our fits were done in a two-step fashion for each target. First, the out-of-transit data for each sector was analyzed separately, and fitted with a GP, plus a jitter term and a flux normalization factor. We then compared the bayesian evidence on each sector for each of the kernels outlined above, and the one that was preferred for most of the sectors was defined as *the* kernel to use for that target. Then, the posteriors on each of these parameters for each sector were used as priors for a multi-sector joint fit of the in-transit data, to which we added the transit model. This two-step process for fitting these transit lightcurves had two main advantages. The first advantage is that this provides a much more efficient sampling of the parameter space given we use nested sampling algorithms to explore it (which are much better behaved in low dimensional spaces). The second advantage, which is a byproduct of the first one,

¹ <https://exoplanetarchive.ipac.caltech.edu/cgi-bin/TblView/nph-tblView?app=ExoTbls&config=planets>

² <https://heasarc.gsfc.nasa.gov/cgi-bin/tess/webtess/wtv.py>

³ <https://mast.stsci.edu/portal/Mashup/Clients/Mast/Portal.html>

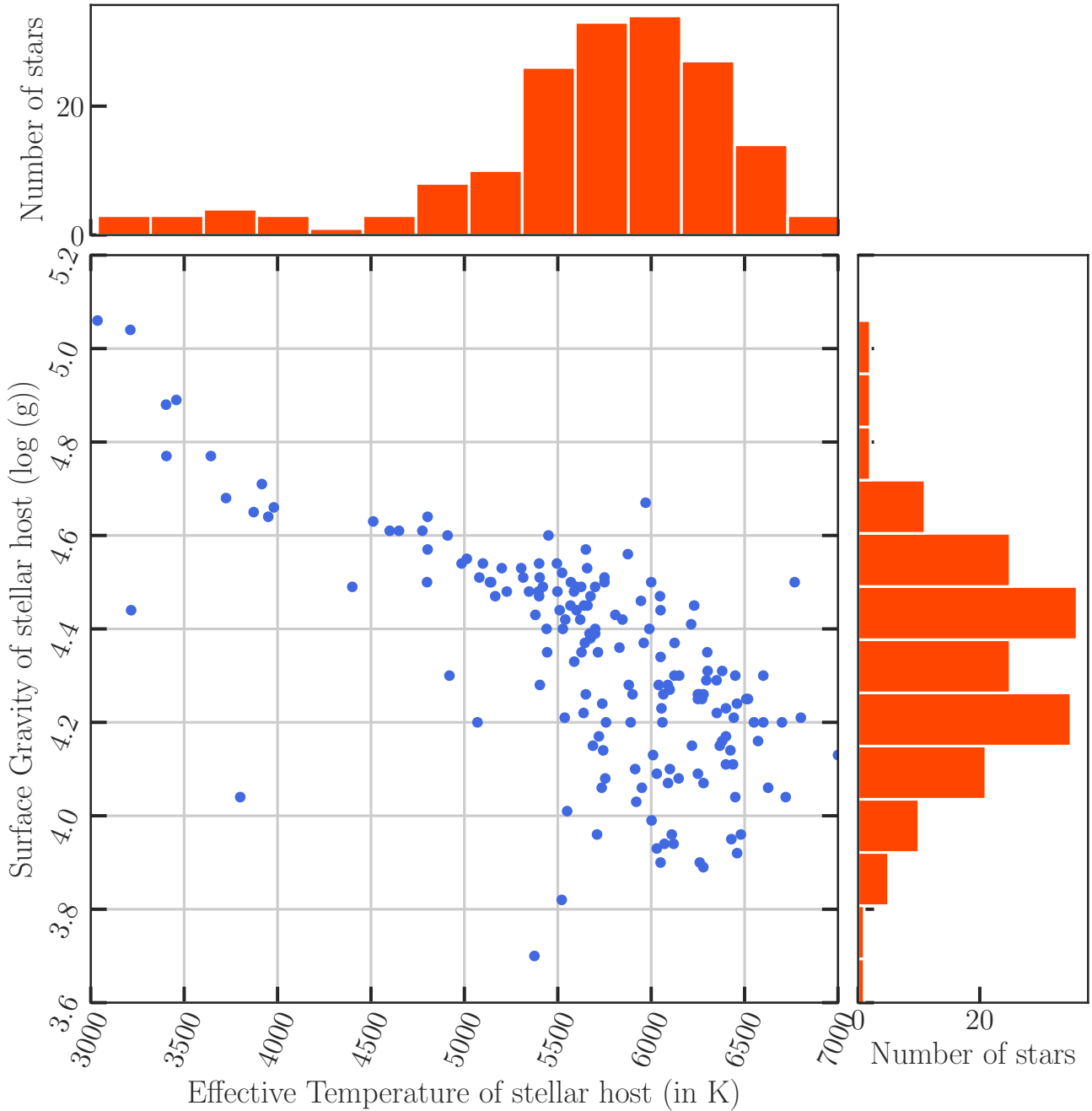


Figure 1. Range and distribution of Effective Temperature (T_{eff}) and Surface Gravity ($\log g$) of target exoplanet host stars.

is that it allows for a much faster convergence of the algorithms. We follow the recommendation in Espinoza et al. (2019a), and use importance nested sampling with the MultiNest algorithm (Feroz et al. 2009) via the PyMultiNest library (Buchner et al. 2014) to perform fits with up to about 20 free parameters, and use dynamic nested sampling via the *dynesty* library (Speagle 2020) to explore higher dimensional parameter spaces. In practice, this means that we use MultiNest for multi-

sector fits involving less than 4 sectors, and *dynesty* for multi-sector fits involving 4 or more sectors. Our automated routines to perform this two-step fitting procedure is available at Github⁴.

The priors used in our fits were, in general, wide enough to explore a vast part of the parameter space.

⁴ <https://github.com/nespinoza/tess-limb-darkening/>

Table 1. Summary of priors used in our analysis. $\mathcal{U}(a, b)$ and $\mathcal{J}(a, b)$ show the uniform and log-uniform distribution between a and b , respectively; $\mathcal{N}(\mu, \sigma^2)$ gives the normal distribution with mean μ and the standard deviation σ . The “*lit*” subscript to symbols means that the value of that parameter is taken from the literature. A single value indicates that the parameter was fixed.

Parameter	Unit	Prior
Planetary Parameters		
P	days	$\mathcal{N}(\mu_{lit}, \sigma_{lit}^2)$
T_0	BJD	$\mathcal{N}(\mu_{lit}, 0.1)$
R_p/R_*		$\mathcal{U}(0., 1.)$
b		$\mathcal{U}(0., 1.)$
a/R_*		$\mathcal{J}(1., 100.)$
eccentricity		ecc_{lit}
ω	deg	ω_{lit}
Instrumental Parameters		
q_1 (transformed LDC)		$\mathcal{U}(0., 1.)$
q_2 (transformed LDC)		$\mathcal{U}(0., 1.)$
m_{flux}	ppm	$\mathcal{N}(0., 10^5)$
$m_{dilution}$		1
σ_w (jitter)	ppm	$\mathcal{J}(0.1, 10000)$
Exponential-Matèrn kernel		
Amplitude of the GP	ppm	$\mathcal{J}(10^{-5}, 10000)$
Timescale (Exp part)	days	$\mathcal{J}(0.001, 100)$
Timescale (Matèrn part)	days	$\mathcal{J}(0.001, 100)$
Quasi-Periodic kernel		
B		$\mathcal{J}(10^{-5}, 10^3)$
C		$\mathcal{J}(10^{-5}, 10^4)$
L	days	$\mathcal{J}(10^{-3}, 10^3)$
P_{rot}	days	$\mathcal{J}(1., 100.)$

The only exception was the period of the orbits, whose priors were normal distributions with means and standard deviations taken from previous works in the literature — our posteriors on this parameter, then, can be seen effectively as an update over those previous estimates. The time-of-transit center also had a more or less constrained prior; we also defined a normal distribution as a prior on this parameter based on previous works, but the standard deviation of this distribution was set to 0.1 days (i.e., about 2.4 hours). To parametrize the limb-darkening we decided to use the widely used quadratic law via the uninformative sampling scheme proposed by Kipping (2013). In this setup, instead of fitting for the limb-darkening coefficients directly, we fit for the transformed parameters q_1 and q_2 , each of which we define to

have a uniform prior distribution between 0 and 1. We defined wide priors between 0 and 1 for the planet-to-star radius ratio and the impact parameter of the orbits. For a/R_* , the scaled semi-major axis, we decided to use a wide log-uniform prior between 1 and 100. In order to account for possible out-of-transit offsets, we also fitted for a mean out-of-transit flux in our transit fits, m_{flux} , which normalizes the lightcurve via $1/(1 + m_{flux})$ (see Espinoza et al. 2019a, for details); we defined a normal prior for this parameter with zero-mean and a standard deviation of 10^5 ppm. A dilution factor was set to 1 for all of our fits (i.e., assuming no dilution by nearby sources), as most of our targets are bright and the PDC algorithm is supposed to correct for the dilution of nearby objects anyways. Finally, for our GP kernels, we also defined wide priors. For the Exponential-Matèrn kernel, we used a log-uniform prior on the amplitude of the GP from 10^{-5} to 10,000 ppm, and time-scales for both the exponential and Matèrn parts of the kernel between 0.001 and 100 days. For the quasi-periodic kernel, the B, C and L parameters had log-uniform priors between 10^{-5} to 10^3 , 10^{-5} to 10^4 , and 10^{-3} to 10^3 . The rotation period of the kernel had a log-uniform prior between 1 and 100 days. All lightcurve models also included a white-gaussian zero-mean noise component, whose standard deviation was also fitted in our procedure. The prior for that “jitter” parameter was defined to be log-uniform between 0.1 and 10,000 ppm. The eccentricity and argument of periastron on our fits was fixed to literature values.

We also note here that although our target list consist of already known exoplanets observed by TESS up to Sector 32, we downloaded *all* available data for these targets, which may include, for some of the systems, data from the most recent data release of Sector 34.

2.3. Theoretical calculation of Limb Darkening Coefficients

One of the key parts of our work involves computing theoretical LDCs in order to compare them with our empirical estimates obtained from *TESS* lightcurve fits. In this work, we used two main methods to compute these. The first, and the most popular method used by the community, is to use various tables/codes published in the literature to directly retrieve those coefficients. These coefficients, in turn, are obtained by fitting the intensity profiles of model stellar atmospheres, weighted by the instrumental bandpasses (see, e.g., Claret et al. 2012; Espinoza & Jordán 2015). The second method we use is the one suggested by Howarth (2011): the Synthetic-Photometry/Atmosphere-Modelling (or, SPAM) technique. This is a technique explicitly de-

signed to work with exoplanetary transit lightcurves, and involves generating synthetic transit lightcurves with limb-darkening coefficients estimated from the same tables/codes as the ones described above, which are then fitted with a limb-darkening law of choice to retrieve the LDCs. We detail how we explicitly obtain the LDCs we use in this work with these two methods below.

2.3.1. LDCs from Tables/Codes

In order to perform theoretical predictions for LDCs obtained from our lightcurve fits, we made use of limb-darkening tables and/or algorithms present in the literature that use both ATLAS and PHOENIX model stellar atmospheres as inputs. To put all those predictions on equal footing and to maximize the amount of information extracted from those tables, instead of extracting tabulated quadratic limb-darkening coefficients we followed the approach of Espinoza & Jordán (2015), in which “limiting” limb darkening coefficients are derived using the non-linear law. This approach guards against the fact that different models and methods to fit for the intensity profiles of model stellar atmospheres give rise to slightly different results depending on the number of points sampled from those profiles. In essence, the method simply performs χ^2 - minimization between the non-linear law and the quadratic law, to find a relationship that gives the quadratic limb-darkening coefficients as a function of the non-linear limb-darkening coefficients (see Espinoza & Jordán 2015, for a derivation), which is given by:

$$\begin{aligned} u_1 &= \frac{12}{35}c_1 + c_2 + \frac{164}{105}c_3 + 2c_4 \\ u_2 &= \frac{10}{21}c_1 - \frac{34}{63}c_3 - c_4. \end{aligned} \quad (2)$$

Here c_1 , c_2 , c_3 and c_4 are the LDCs of the non-linear law, and u_1 and u_2 are the resultant “limiting” LDCs for the quadratic law. We use these latter ones to compare our retrieved limb-darkening coefficients from our transit fits.

We retrieve theoretical LDC calculations on the *TESS* bandpass for our targets using two different sources/methods. The first set is obtained using the `limb-darkening`⁵ code outlined in Espinoza & Jordán (2015). The second are the tables published by Claret (2017), which are arguably very popular among researchers that analyze *TESS* data.

There are several details and/or assumptions one has to be careful with when dealing with those sources of

LDCs, which we here pay attention to when comparing them against our empirically determined LDCs using *TESS* lightcurves. The first is that, as put forward by Wittkowski et al. (2004), ATLAS and PHOENIX model stellar atmospheres disagree about where the stellar atmosphere ends, which in turn implies that different results between both are practically guaranteed if not accounted for. Different authors have approached this problem in different ways. On the one hand, Espinoza & Jordán (2015) follow Wittkowski et al. (2004) and look for an inflection point in the intensity profile of spherically symmetric models (i.e., where the derivative of the intensity as a function of $r = \sqrt{1 - \mu^2}$ reaches its maximum), redefining that point to be at $r = 1$ (i.e., $\mu = 0$). Claret (2017), on the other hand, suggests that a “better” approach — where “better” is defined as attaining a lower residual sum of squares with respect to the fitted intensity profile (see their Figure 1) — is to simply not use values where $\mu < 0.1$, a method they refer to as the “quasi-spherical” method. Those two methods are fundamentally different approaches, and it is furthermore unclear which one of those is better (or if they can be even distinguished with actual data). In order to attempt at testing their efficacy at predicting empirically determined LDCs, here we extract LDCs from the tables of Claret (2017) using both methods. Following that same study, in this work we refer to the former as the *r-method*, and to the latter as the *q-method*.

The second important detail has to do with the fact that Espinoza & Jordán (2015) used the “vanilla” PHOENIX - COND models, available from the PHOENIX website⁶. Claret (2017), however, suggested that their work uses slightly different versions of those models (the ones from Claret et al. 2012), and that furthermore, discrepancies between the works of Claret et al. (2012) and Espinoza & Jordán (2015) for stars with effective temperatures lower than 3000 K could be explained due to Claret et al. (2012) using PHOENIX-DRIFT models. While the latter cannot be tested with the data obtained in this work (as none of our stars has effective temperatures smaller than 3000 K), the impact of the slightly different PHOENIX-COND models used by these authors *can* be tested, by paying attention to the prediction error between the tables of Claret (2017) using the *q-method* and the predictions made using the `limb-darkening` code of Espinoza & Jordán (2015), which for PHOENIX use the *r-method* by default. Here, thus, we also take the opportunity to test which of these versions of the PHOENIX mod-

⁵ <https://github.com/nespinoza/limb-darkening>

⁶ <ftp://phoenix.astro.physik.uni-goettingen.de/SpecIntFITS/>

els is actually preferred to minimize mismatches with actual empirical LDCs obtained from *TESS* lightcurves.

2.3.2. Synthetic-Photometry/Atmosphere-Model LDCs

Obtaining LDCs from fits to model intensity profiles is an inherently different optimization problem to that of obtaining LDCs from fits to transiting exoplanet lightcurves. They have different optimization functions as they are optimizing different supposed observables. As shown by Howarth (2011), this fact may give rise to completely different LDCs, depending on the adopted fitting method, even if the same coefficients are used to generate both the intensity profile and the transiting exoplanet lightcurve. In order to take this into account when comparing theoretical to empirically obtained LDCs through transit lightcurve fitting, Howarth (2011) proposed an alternative way of computing theoretical LDCs: the Synthetic-Photometry/Atmosphere-Model (SPAM).

The first step of the SPAM algorithm is to calculate a “synthetic” transit lightcurve with an accurate representation of the stellar intensity profile (in the case of the present work, described by the non-linear law) assuming full knowledge of planetary and stellar properties (although this can be relaxed; see Espinoza & Jordán 2015). This synthetic transit lightcurve is then fitted by a lightcurve model with fixed planetary properties and any limb-darkening law of interest with free LDCs. The retrieved LDCs through this procedure are the SPAM LDCs. Here, we follow this latter procedure by fitting the synthetic lightcurves with a *quadratic* limb-darkening law. We use the ExoCTK⁷ (Bourque et al. 2021) package to compute the SPAM LDCs using the non-linear LDCs derived from the various stellar model atmospheres discussed in Section 2.3.1.

3. RESULTS

Having fitted the *TESS* transit lightcurves of the 176 transiting exoplanets in our sample, we are now in a position to compare the empirically obtained LDCs with the theoretical ones described in the previous section. In what follows, we present these results in two parts. In the first part, we compare the retrieved planetary parameters obtained from our *juliet* fits to the *TESS* data with their corresponding literature values in order to validate our modelling procedure. Then, we compare the retrieved LDCs from those transit fits with the ones calculated theoretically from model stellar atmospheres

obtained as discussed in Section 2.3. The codes which we used to produce all the results in this section are publicly available on Github⁸.

3.1. Comparison with literature values

Our *juliet* fits allow us to estimate various planetary parameters along with the limb darkening coefficients. The former, in turn, provide us with an excellent dataset which is useful not only to refine these planetary parameters, but also to validate our procedures by comparing them to the ones already estimated in the literature. While such a validation in principle assumes these literature values are unbiased, we believe the risk of this not being the case is somewhat mitigated by the wide range of instruments, analyses and assumptions made by different authors that analyzed these systems in the past. To perform this comparison, we chose three planetary parameters to compare in this work, which are the ones for which we obtain the most precise constraints: the scaled semi-major axis (a/R_*), the planet-to-star radius ratio (R_p/R_*) and the time of transit center (t_c).

Before presenting the main results of our study for all the planets in our sample, we first present a representative fit for the WASP-62b system as observed by *TESS* (including all sectors on which this exoplanet was observed). The summary of this fit is presented in Figure 2. As can be seen, the phase-folded transit lightcurve has exquisite precision, and doesn’t give rise to any noticeable leftover signal in the residuals. Indeed, a power spectral density analysis reveals no significant signals are present in the residual time-series, suggesting our Exponential Matern kernel did take care of any correlated noise structure in the data. In terms of achieving the photon-noise level of these observations, for some sectors a significant jitter term of a couple of hundreds of ppm is found. This is the case for Sector 1, 4, 7, 8 and Sector 27 through 34. This probably points to the fact that the PDC algorithm has some extra uncorrected systematics in those sectors, but the amplitude seems to be overall small and, judging from our power spectral density analysis, it is unimportant in terms of correlated noise in the time-scales of interest for our analyses (\sim hours). The posterior distribution of the transit lightcurve parameters for this target are presented in Figure 3, where we have transformed the q_1 and q_2 limb-darkening parameters back to the u_1 and u_2 plane using the transformations in Kipping (2013). These posterior parameters, in turn, are in very good agreement with previous values

⁷ <https://github.com/ExoCTK/exoctk>
see also, <https://github.com/Jayshil/ld-spam/blob/main/p2.py>
for our implementation

⁸ <https://github.com/nespinoza/tess-limb-darkening>,
<https://github.com/Jayshil/ld-project-updated>, and,
https://github.com/Jayshil/my_thesis

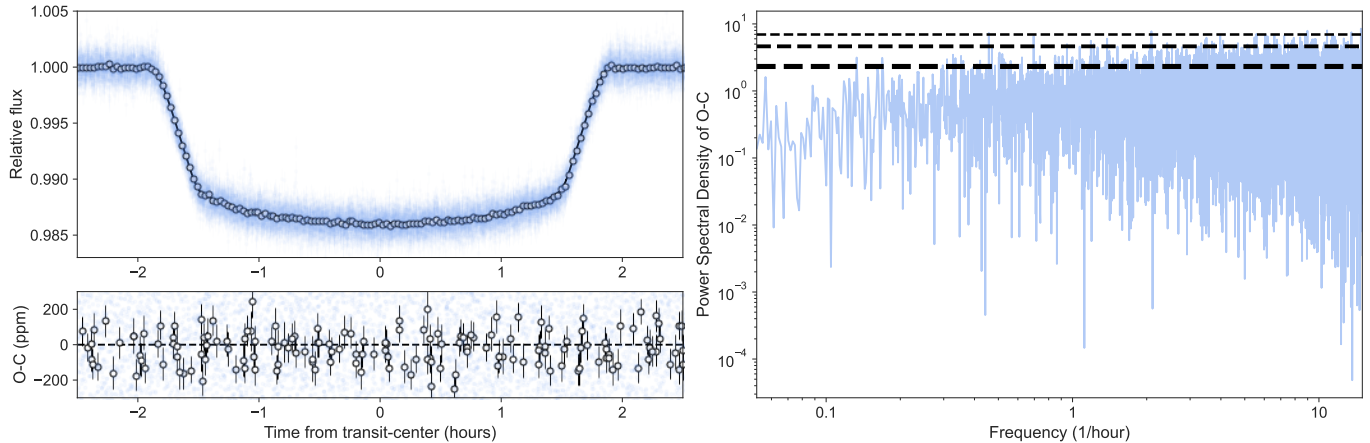


Figure 2. (*Left*) Phase-folded lightcurve for the systematics-removed WASP-62b system with data taken by TESS combining the observations of all sectors (top left plot; blue datapoints), and the residuals from the best-fit model (bottom left plot). The white circles with black errorbars are binned datapoints in 2-minute intervals in this phased lightcurve. (*Right*) Power spectral density (PSD) of the residuals of the best fit, which doesn’t show any significant signal on the frequencies relevant to the transit event. Dashed lines from top to bottom show where 99.9%, 99% and 90% of the PSD of simulated gaussian noise with the same properties at those of the errorbars on our data falls; the observed PSD of the residuals falling below these lines suggests it is consistent with that of white gaussian noise).

in the literature. For instance, the planet-to-star radius ratio (R_p/R_*) from our fits is 0.1111 ± 0.0001 , which is within $3 - \sigma$ from the value found by Maciejewski (2020) of 0.1105 ± 0.0003 . A similar agreement is found for the rest of the transit parameters: our estimated scaled semi-major axis (a/R_*) is 9.72 ± 0.03 , which is within 1-sigma from the value found by Stassun et al. (2017a) of 9.55 ± 0.41 . Finally, the difference between the transit center predicted by that same work on the timespan of the *TESS* observations and the one estimated by our transit fits are also in very good agreement agreement — they show a difference of 28.757 seconds, which is consistent with zero within 1-sigma. The predicted ephemerides from the work of Bonomo et al. (2017) has considerably deteriorated since its publication, showing a bias of around 12 minutes for this target. Our *TESS* updated ephemerides, however, significantly improve its precision to only 3 seconds.

The same comparison on the retrieved transit parameters done above for WASP-62b is presented for *all* the targets in our sample in Figures 4, 5 and 6. Literature values for the planetary parameters were obtained from the NASA Exoplanet Archive, as queried on February 23, 2021. The comparison is also presented in Table 6. Our results show in general very good agreement with literature values. There are, however, a set of 25 exoplanetary systems in our sample for which we find that one or more than one of the planetary parameters compared in Figures 4, 5 and 6 (i.e., the time-of-transit center, a/R_* and/or R_p/R_*) are at least $3 - \sigma$ away from what is published in the literature. A de-

tailed, case-by-case analysis is presented in Appendix A for those systems, but we found that for 19 of them we are confident our retrieved values are updates over previous published values for these parameters, and that for 5 of them the most likely explanation is either stellar activity variations producing slight transit-depth variations, real planetary variability in the transit depths and/or mismatches on the dilution factors applied by the *TESS PDC* pipeline. The only target in which we consider the methods here presented failed to retrieve the correct properties is LTT9779 b, for which we sample a discrepant solution to the one described in Jenkins et al. (2020) with our methodology. This solution was actually briefly discussed in Jenkins et al. (2020), but was discarded as the implied stellar density does not agree with the spectroscopic one observed in that work. Overall, we consider having only 1 outlier out of a sample of 176 targets is in fact a very good result, which in turns gives us confidence in our lightcurve analysis procedures.

Before moving on with our results, we would like to highlight the curious case of the WASP-140 b exoplanetary system, which has a nearby but not physically associated bright star. There are many systems in our sample that have such companions, and our hypothesis on such targets was that, while they would dilute the transit signal, the *PDC* lightcurves should have accounted for these dilutions in the final reported fluxes. However, it seems the correction in the case of WASP-140 b was either not appropriate or not sufficient to account for it based on a comparison of our original lightcurve fits

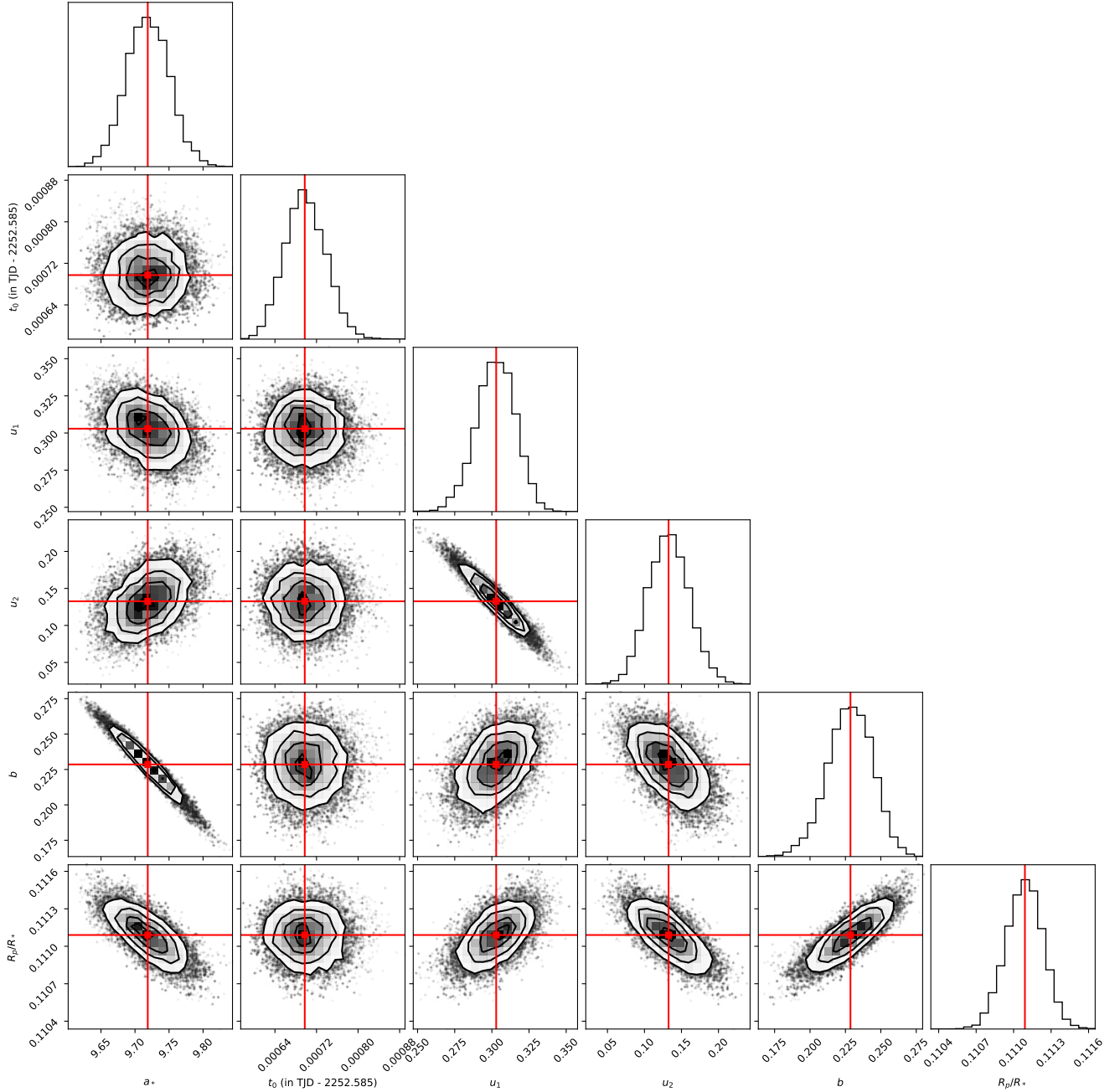


Figure 3. Corner plot of various retrieved parameters for WASP-62b system

with those published in the literature by [Hellier et al. \(2017\)](#). We thus decided to take care of this dilution via the so-called dilution factor in the modelling process (see [Espinoza et al. 2019a](#)). Instead of fixing this dilution factor in the modelling procedure to 1, as done for the rest of the targets, we fit it together with the rest of the transit parameters. Our results, however, still were inconsistent with those of [Hellier et al. \(2017\)](#) even if accounting directly for this dilution. Our fixed dilution

fit gives rise to a planet-to-star radius ratio which is over 60% larger than the one reported by [Hellier et al. \(2017\)](#) — and to a much larger radius if the dilution is left as a free parameter. In both cases, the impact parameter we retrieve is $b > 1$ at 5-sigma, which although a couple of sigmas away from the value reported in that study ($b = 0.93^{+0.07}_{-0.03}$) is still consistent with it in our fixed dilution case. We believe that a full joint analysis of the entire photometric and radial-velocity datasets for

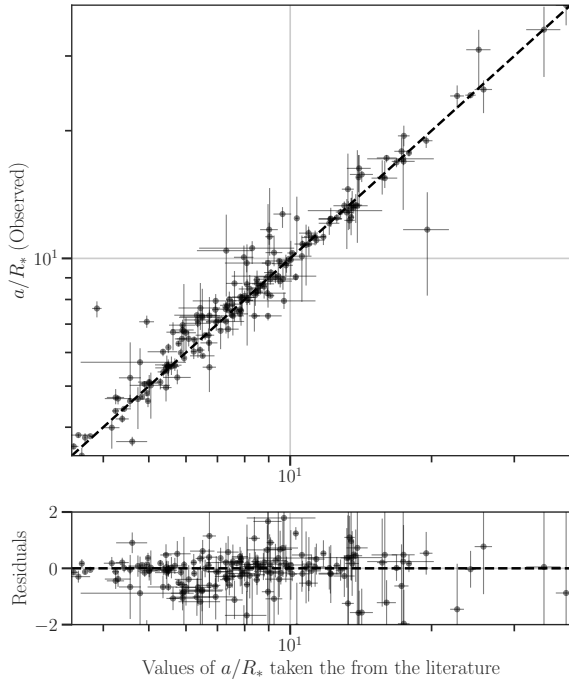


Figure 4. Comparison of the scaled semi-major axis (a/R_*) calculated using `juliet` with its corresponding literature values. The observed values and the values from the literature are on the y-axis and x-axis respectively in the upper panel, while the lower panel shows the residuals between those two values.

this system is needed in order to solve this discrepancy, but we leave such an analysis for future work. Here, we simply discard this system from our analysis.

3.2. Analysis of targets in multiple sectors

An additional good consistency check for the results presented in this work is to perform a thorough analysis of exoplanetary systems that had data spanning multiple sectors. This allows us to test our methods in virtually independent datasets of the same systems which not only allows us to compare the retrieved transit parameters among different sectors, but also extract the most precise LDCs in our sample by combining the datasets at hand. For our analysis we decided to use all the data available for those systems up to Sector 34, which implies some of them had observations in sectors more recent than the ones we selected to define our target sample. In our case, these datasets were the ones for WASP-62 (20 sectors), TOI-481 (9 sectors), WASP-119 (12 sectors), LHS1815 (20 sectors), TOI-157 (12 sectors), WASP-79 (4 sectors) and HATS-46 (4 sectors).

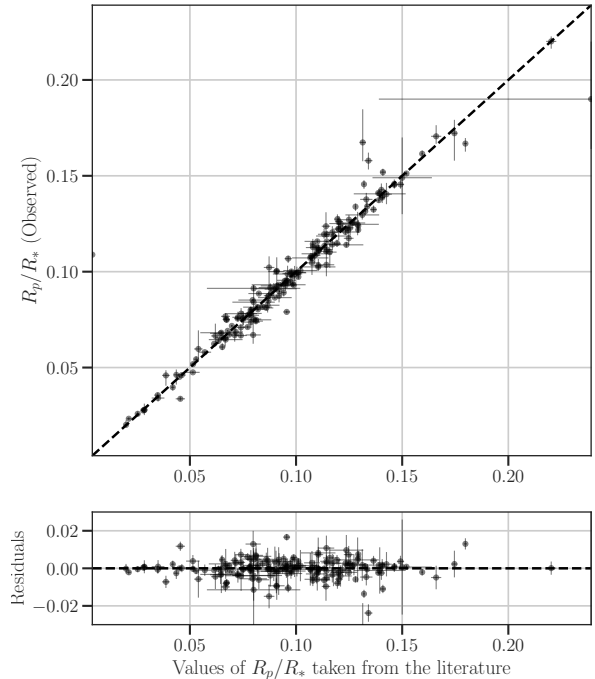


Figure 5. Comparison of the planet-to-star radius ratio (R_p/R_*) calculated using `juliet` with its corresponding literature values. The observed values and the values from the literature are on the y-axis and x-axis respectively in the upper panel, while the lower panel shows the residuals between those two values.

In Figure 7, we present our lightcurve fit results for WASP-62b in different sectors, alongside with the corresponding transit depths. The sector-by-sector fits were performed with the Exponential-Matèrn GP kernel. As can be seen, the transit depths are mostly consistent between sectors and they actually converge to the same value that is found in the literature. The only significantly discrepant value is that of Sector 31, which has a transit depth of 12687 ± 97 ppm — ~ 3 -sigma away from the combined transit depth. Interestingly, our analyses show that the discrepancy in this case is mostly driven by the selection of the GP kernel: a quasi-periodic kernel fit on this particular sector (which gives a much better bayesian evidence) gives back a transit depth of 12376 ± 129 ppm; consistent with the combined depth. While this would hint that we should perhaps allow different GP kernels to be fit on different sectors, we found that for the combined multi-sector analysis we perform in this work this extra complexity is not important, as we obtain the same results either way. Not considering Sector 31, we ran a chi-square test comparing the ob-

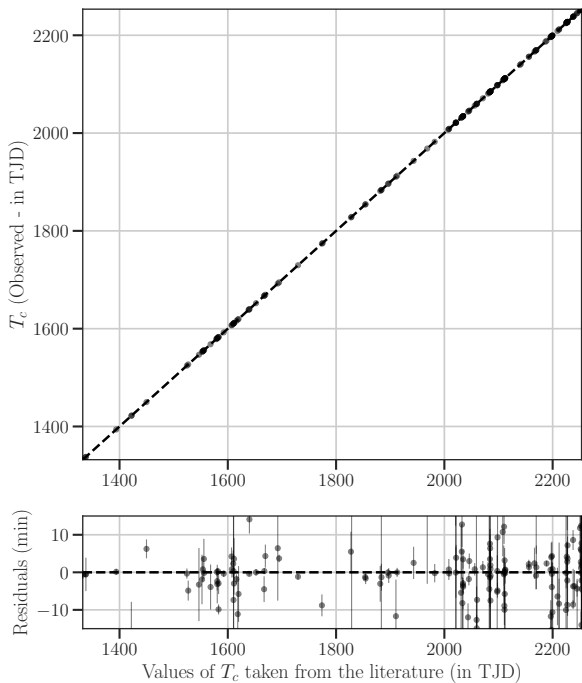


Figure 6. Comparison of the time of transit center (t_c) calculated using `juliet` with its corresponding literature values. The observed values and the values from the literature are on the y-axis and x-axis respectively in the upper panel, while the lower panel shows the residuals between those two values.

served depths and errors from all sectors to that of the mean depth across all of them. This gave back a p-value of 0.34 — with which we fail to reject the null hypothesis that the data is consistent with gaussian noise. This is good evidence that, indeed, the transit depths are constant accross sectors, and consistent with the value found in the literature. As can be seen in Table 6, the same applies to all the other planets observed in multiple sectors. This gives us confidence that our analysis is also well behaved between sectors.

The corresponding limb-darkening coefficients extracted from the transit lightcurves for those targets are presented in Figure 8, where we plot the observed minus the predicted theoretical limb-darkening coefficients, which we obtained from Espinoza & Jordán (2015), for our targets both using PHOENIX and ATLAS models. As can be seen, the limb-darkening coefficients are largely consistent for the u_1 coefficient, for both ATLAS and PHOENIX models though a small offset is still present. However, for the u_2 coefficients, both models are evidently a poor match to the observations, producing a

comparatively large offset. As we will see below, such discrepancy is not exclusive of the multiple-sector data: this happens with the vast majority of the systems we analyzed.

3.3. Comparison between theoretical and empirical LDCs from TESS

In the previous sections we have performed a detailed comparison between the retrieved planetary parameters with their corresponding literature values, finding very good agreement between the two. We consider these results as a validation that our fits to *TESS* data are indeed adequately constraining the transit lightcurve shapes.

Having validated our results with literature data on the physical planetary parameters (relative to those of the star), we now switch our focus in order to compare the retrieved LDCs with their corresponding theoretical values, obtained as described in Section 2.3. The empirically determined LDCs for each of the targets analyzed in this work as well as their theoretical predictions are presented in Table 4 and Table 5.

We present a system-by-system comparison between the empirical and the theoretical LDCs using the various here outlined procedures in Figures 13 through 18: from Figure 13 through 15 we provide the comparison against theoretical LDCs obtained directly from previously published tables/codes (i.e., following the method described in Section 2.3.1), and from Figures 16 through 18 we present the results following the SPAM methodology for obtaining the LDCs (i.e., following the method described in Section 2.3.2). To further summarize those results, in Figure 9 we present the mean offset between the *TESS* retrieved LDCs and the theoretically predicted ones for both sets of LDCs; these mean offsets are in turn also presented in Table 2.

As can be observed from Figure 9, the general behaviour of the offsets in the LDCs remain the same independent of which method one decides to use to compute the theoretical LDCs. The u_1 coefficients are consistently under-predicted by those theoretical calculations, while the u_2 coefficients are over-predicted. This latter coefficient, however, is the one that shows the largest (absolute) offset accross methods. Perhaps one of the most interesting features of these results, however, is the significantly lower offset the SPAM LDCs show when compared against the empirically obtained LDCs — similarly to what was observed by *Kepler* in the analyses of Howarth (2011) and Espinoza & Jordán (2015). As in those works, this suggests that this is, indeed, on average the correct way of extracting theoretical LDCs for usage in transit lightcurve modelling. LDCs extracted without

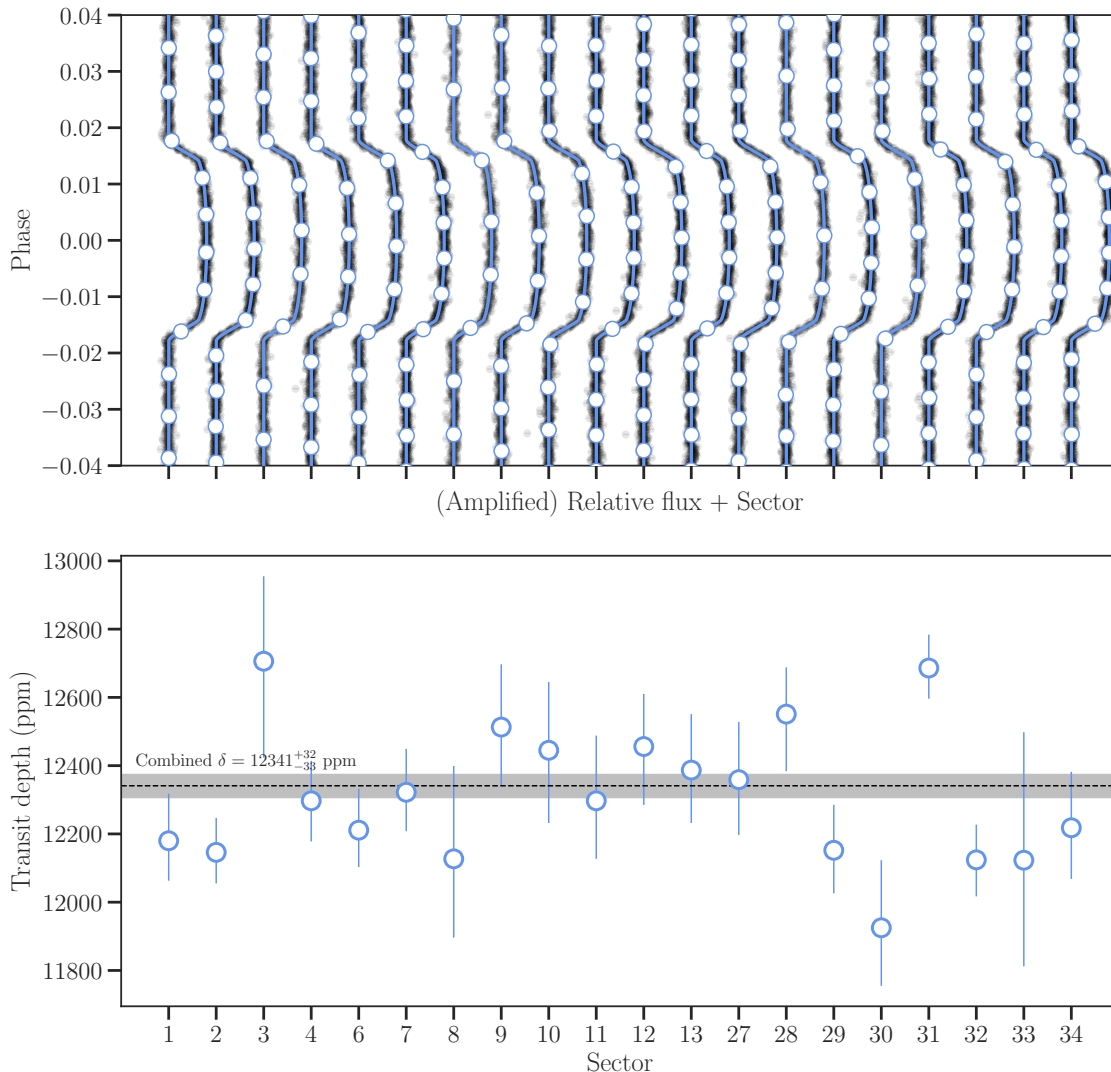


Figure 7. Transit lightcurves (top; black datapoints original data, white points binned data, blue curves best-fit lightcurves) and transit depths (bottom; blue points with errorbars) on each sector for one of our best constrained targets in this work: WASP-62b. As can be seen in the bottom plot, the retrieved transit depths are consistent between sectors, and they converge to a value (12341^{+32}_{-33} ppm; grey band representing this 68% credibility band) which is in agreement with the literature value (12210 ± 66 ppm).

this SPAM algorithm all show significant offsets ($> 3\sigma$) with respect to empirically determined LDCs in at least one coefficient, with the worst performing method being the *q-method* of Claret (2017) which shows a mean offset on the u_2 coefficient of $\Delta u_2 = 0.243 \pm 0.022$ — a very large offset when one considers the space of all possible coefficients for u_2 spans the range from -1 to 1. When applying the SPAM methodology, however, most

of these offsets become consistent with zero at about 2-3 σ levels for both u_1 and u_2 . The exceptions are the LDCs calculated using the *q-method* of Claret (2017, $\Delta u_2 = 0.071 \pm 0.022$) and the ATLAS LDCs, which show significant offsets on both coefficients for both, the calculations made using the Claret (2017) tables or the limb-darkening library of Espinoza & Jordán (2015).

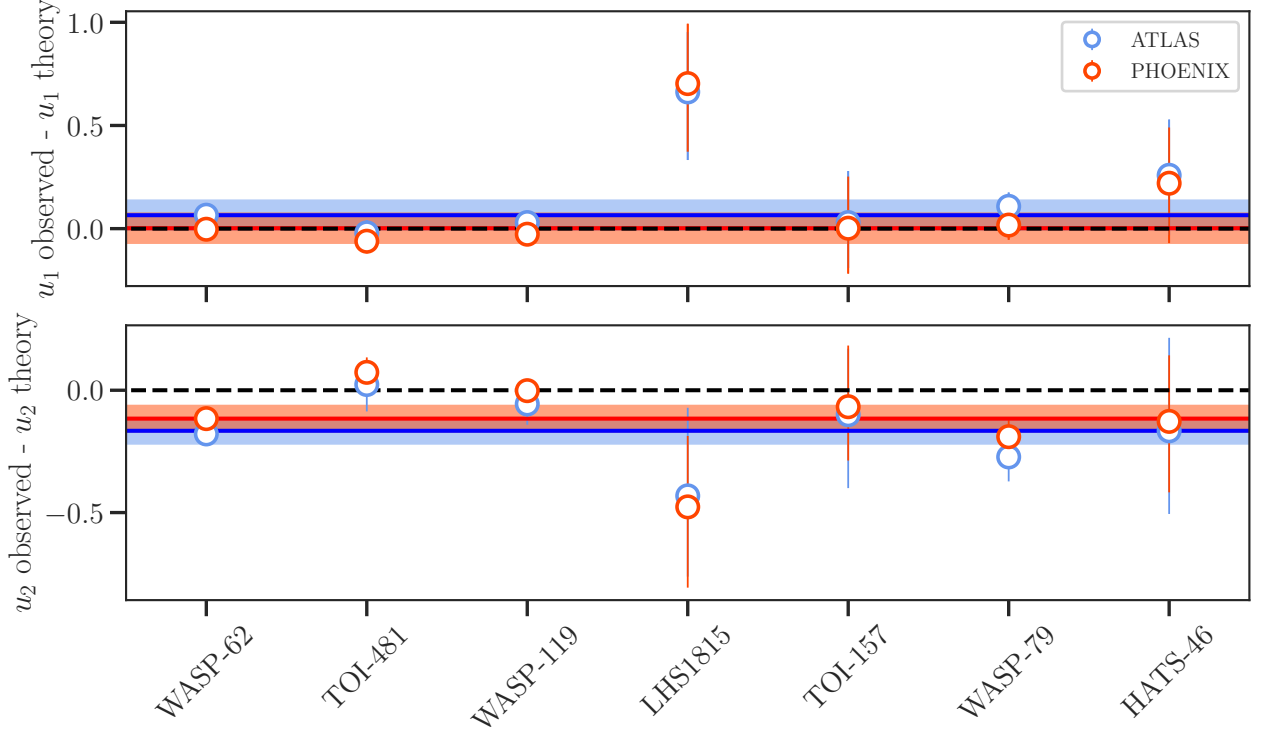


Figure 8. Limb-darkening coefficients extracted for our best-precision targets (the ones spanning data in multiple sectors), compared against their theoretical predictions (blue for ATLAS models, red for PHOENIX). As can be seen, a clear offset is observed for the u_2 limb-darkening coefficient. The bands show the uncertainties in the mean offset with the red and blue colors representing the PHOENIX and ATLAS models. The method to compute theoretical LDCs is the one from [Espinoza & Jordán \(2015\)](#).

Table 2. Mean offset present in the Tabular/Code and SPAM LDCs using PHOENIX and ATLAS model stellar atmospheres with different calculation methods.

Method	Δu_1	Δu_2
Tabular/Code LDCs		
ATLAS (Espinoza & Jordán 2015)	-0.096 ± 0.018	0.145 ± 0.022
PHOENIX (Espinoza & Jordán 2015)	-0.058 ± 0.018	0.107 ± 0.022
ATLAS (Claret 2017)	-0.101 ± 0.018	0.128 ± 0.021
PHOENIX - <i>q-method</i> (Claret 2017)	-0.132 ± 0.018	0.243 ± 0.022
PHOENIX - <i>r-method</i> (Claret 2017)	-0.072 ± 0.018	0.107 ± 0.022
SPAM LDCs		
ATLAS (Espinoza & Jordán 2015)	-0.075 ± 0.018	0.101 ± 0.022
PHOENIX (Espinoza & Jordán 2015)	-0.019 ± 0.018	0.044 ± 0.021
ATLAS (Claret 2017)	-0.084 ± 0.017	0.093 ± 0.022
PHOENIX - <i>q-method</i> (Claret 2017)	-0.034 ± 0.018	0.071 ± 0.022
PHOENIX - <i>r-method</i> (Claret 2017)	-0.020 ± 0.018	0.042 ± 0.022

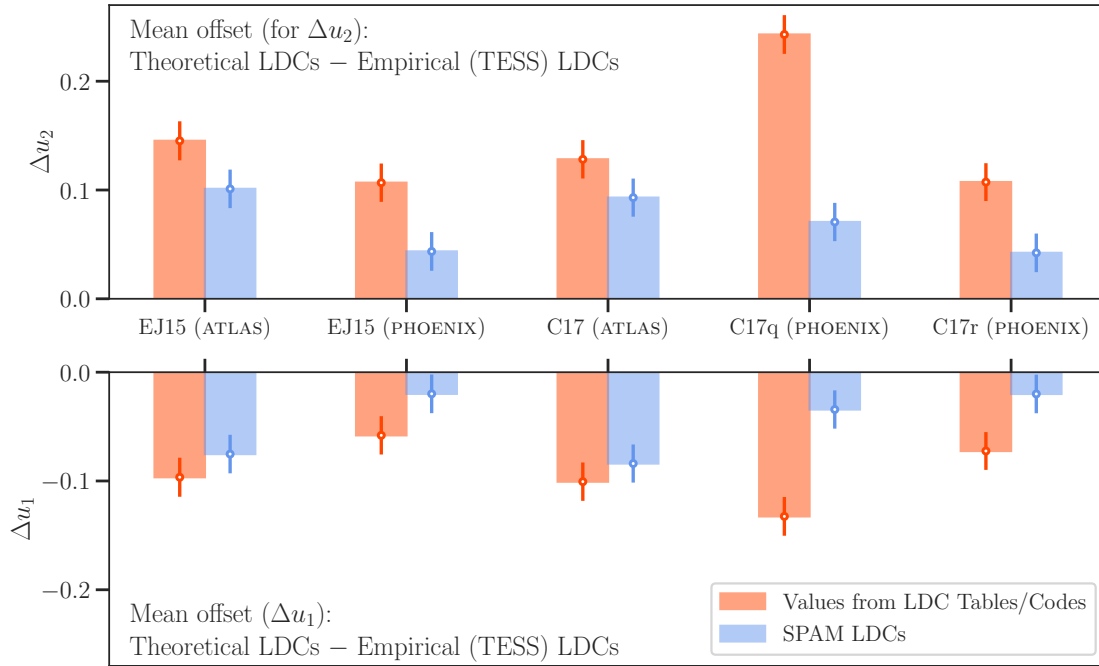


Figure 9. Mean offset between empirically determined LDCs (through *TESS* transiting exoplanet lightcurves) and the theoretically derived LDCs when using a quadratic law. Different colors of the bars represent the different methodologies to compute theoretical LDCs, from LDCs Tables/Codes (Section 2.3.1, orange) and SPAM LDCs (described in Section 2.3.2, blue). The x-axis shows the various origins of these theoretical LDCs: the work of Espinoza & Jordán (2015, EJ15) and the work of Claret (2017, C17). The additional suffix for this latter work (q and r) represent two different sets of assumptions used by Claret (2017) to obtain these LDCs (see text for details). The top panel shows the offset for the u_2 coefficient while the lower panel shows the offset for the u_1 coefficient of the quadratic law.

4. DISCUSSION

The results presented in the previous section and summarized in Figure 9 seem to suggest two main take-home messages. First, when using quadratic LDCs extracted directly from limb-darkening tables, large offsets as large as $\Delta u_1 \approx -0.1$ and $\Delta u_2 \approx 0.2$ can be expected, on average, with empirically determined LDCs in the *TESS* bandpass, with the offsets being worse for the PHOENIX models than for the ATLAS models (top set of values in Table 2). If one uses the SPAM methodology to obtain these LDCs, however, these offsets reduce, on average, to virtually zero for LDCs obtained using the PHOENIX stellar models and the *r-method* with both the tables published by Claret (2017) and the limb-darkening library of Espinoza & Jordán (2015) (see bottom set of values in Table 2). This, in turn, suggests the SPAM methodology is the one that should be adopted by default when using theoretical LDCs to perform transit lightcurve modelling in the *TESS* bandpass, in particular using that technique together with PHOENIX stellar model atmospheres.

These take-home messages, however, do not tell the entire story of the observed offsets between theoretically and empirically determined LDCs. Given different stars have different limb-darkening profiles, we must be careful with interpreting these results especially considering the overabundance of F and G-type stars in our sample. With this motivation in mind, we discuss the variation of these offsets with host star temperature in the next sub-section.

4.1. Variation in offset with effective temperature of the host star

As described in the previous section, there are suggestions of mean offsets when comparing empirical to theoretically determined LDCs. The works of Müller et al. (2013b) and Espinoza & Jordán (2015), in turn, when performing a similar analysis on *Kepler* lightcurves, observed a possible dependence of those offsets with stellar temperature. Motivated by this, we here explore that dependence using our *TESS* LDCs in what follows.

To check for any such possible dependencies, we plot the residuals between the theoretical and the *TESS* retrieved LDCs as a function of the effective temperature for both sets of theoretical LDCs (those derived from limb-darkening Tables/Codes and the SPAM LDCs) in Figures 10 and 11 for the representative case of the Espinoza & Jordán (2015) LDCs (which are fairly similar to the ones tabulated by Claret (2017) using the

*r-method*⁹.) To find any possible correlation between these offsets and the effective temperature of the host stars, we fit those residuals with polynomials ranging from zeroth (i.e., a constant model) to second order. We used the Bayesian Information Criterion (BIC; Schwarz 1978) to determine the best fitting model among those three models, and present the best of them (i.e., the one with the minimum BIC) in Figures 10 and 11 with dashed-dotted lines.

In almost all of those residual plots we find a quadratic function seems to fit the residuals best, with the vertex of the parabola touching (or being close to) zero at about 6000 K. The residuals, in turn, seem to increase their absolute values as they go to cooler and hotter stars. For instance, for the PHOENIX models, these quadratic functions predict offsets of order ≈ 0.2 for both SPAM and non-SPAM coefficients. Indeed, the SPAM LDCs seem to significantly flatten those parabolas, but indeed, the LDCs especially for cooler stars don't seem to be consistent with zero. This suggest that independent of the methods, LDCs for stars cooler than about 5000 K are not predicted very precisely by our modelling efforts, and thus care must be taken when using theoretical LDCs for stars at those temperatures.

While interpreting these correlation between the effective temperature and the offsets, one needs to keep in mind that the distribution of our sample is not uniform in the effective temperature, as shown in Figure 1 – these distribution shows the deficiency of targets at low and very high temperatures. Still, it is interesting to see how the residuals between theoretical and observed LDCs seem to be better at temperatures close to that of the Sun, which makes intuitive sense given most stellar model atmospheres have been extensively tested against the Sun.

4.2. Limitations of our study

An important limitation of our study to have in mind is the fact that our work requires, by construction, a layered approach to obtaining limb-darkening coefficients from stellar model atmospheres. In other words, the comparison is not direct to the models, but involves a series of assumptions and methods that lead to the final coefficients we compare against the data. As such, it is somewhat complicated to make direct statements about the *actual validity of the stellar model atmospheres* tested in our work. For instance, while we observe that the PHOENIX coefficients obtained through

⁹ For completeness, we show the same plots for the LDCs obtained using the tables in Claret (2017) in Figures 19 through Figure 22) in the Appendix

For Tabular/Code LDCs

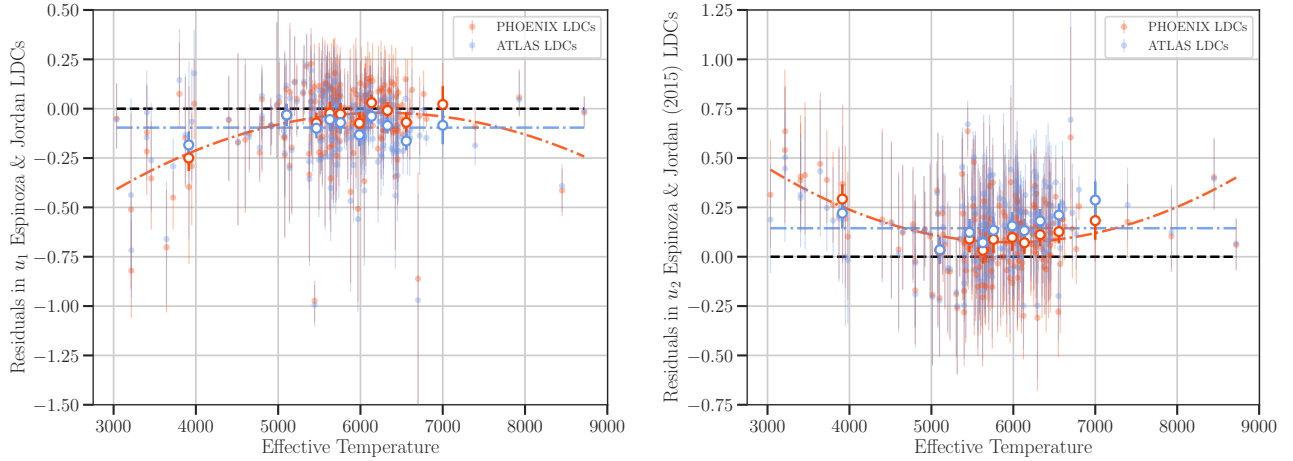


Figure 10. Temperature variation of offsets in u_1 and u_2 , when, theoretically, LDCs are calculated using code provided by Espinoza & Jordán (2015). The dashed-dotted lines show the best fitted model to the residuals.

For SPAM LDCs

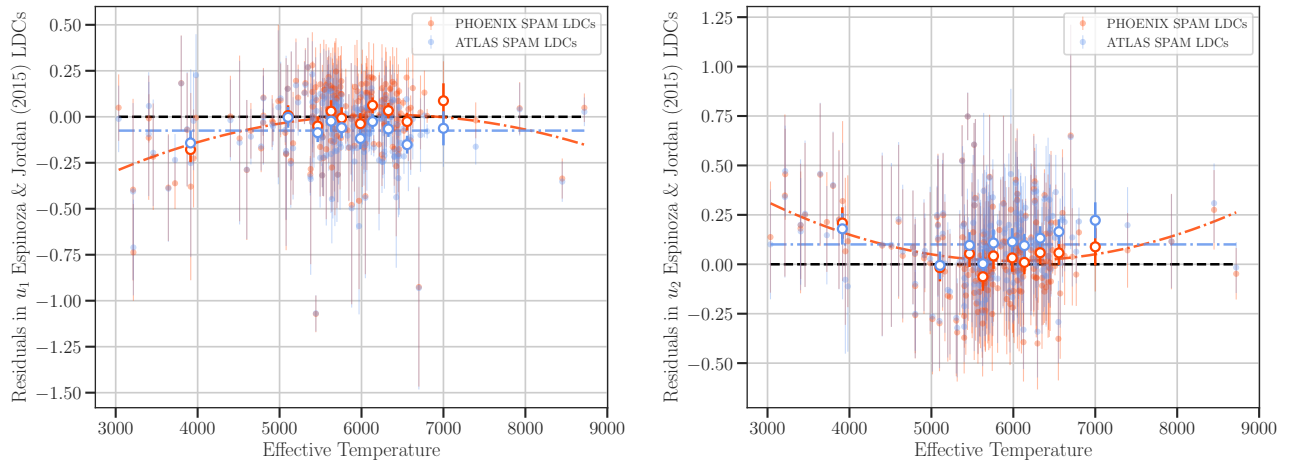


Figure 11. Same as Figure 10, but now using SPAM LDCs.

the r-method behave better when compared against our retrieved empirical LDCs, we cannot confirm if this is because some bias cancels out between the methodology and the actual stellar model atmospheres, or because the stellar models are inherently reasonably well behaved in the *TESS* bandpass, and the r-method is intrinsically better. We can, however, make the *practical* suggestion that, when confronted with the data, and if willing to use tabulated LDCs, one should prefer this method if using the PHOENIX models over the q-method proposed by Claret (2017).

5. CONCLUSION AND FUTURE WORK

In this paper, our main goal was to study the limb darkening of exoplanet host stars using *TESS* transit-

ing exoplanet lightcurves. To achieve this goal, we used precise exoplanet transit lightcurves obtained by *TESS* for 176 known exoplanetary systems, for which we computed limb-darkening coefficients — the primary products needed to meet our work’s goal. A secondary but not less important product of our work are updated transit parameters for these exoplanetary systems. A subset of those (R_p/R_* , a/R_* and the time-of-transit centers) were compared with their corresponding values from the literature with which we found very good agreement. This not only provides a valuable validation of our transit lightcurve fits, but also a rich dataset for the community to use to, e.g., use as prior in precise follow-up observations of these systems, or to even plan observa-

tions of these systems given the improved precision of our ephemerides for most of our studied systems.

We used these results to test how well the limb darkening effect is modelled by current methodologies and stellar model atmospheres. We compared the retrieved LDCs with both ATLAS and PHOENIX model predictions calculated by two authors, Claret (2017) and Espinoza & Jordán (2015) for one of the most widely used limb-darkening laws: the quadratic law. We found significant offsets on the limb-darkening coefficients u_1 and u_2 of the quadratic law between empirically and theoretically determined LDCs, which can be as large as $\Delta u_1 \approx 0.1$ and $\Delta u_2 \approx 0.2$, depending on the methodology and the stellar model atmospheres used for the calculations. Our main take-home message is that the most accurate LDCs for the *TESS* bandpass are the ones that use the SPAM algorithm proposed in Howarth (2011), and which use the PHOENIX model atmospheres using the technique introduced in Wittkowski et al. (2004) and used by Espinoza & Jordán (2015) to calculate limb-darkening coefficients for these stellar model atmospheres — the *r-method* in the terminology used in the published tables of Claret (2017).

Our analysis, however, suggests that even with the “right” methodology, large offsets between theoretical and empirically determined LDCs could be observed for stars cooler than about 5000 K. Below these temperatures, there seem to be offsets as large as $\Delta u_i \sim 0.2$ for the LDCs of the quadratic law. We believe an important future avenue would be to extend our work to a larger sample of exoplanetary systems orbiting cooler stars in order to confirm this trend. The newest of *TESS* dis-

coveries are indeed paving the way to form such a sample, which we believe would be fundamental not only to understand the physical properties and architectures of these exoplanetary systems, but also to understand the limitations of current models and methodologies at predicting the imprint of the limb-darkening effect on real transit lightcurves.

ACKNOWLEDGEMENTS

We would like to thank an anonymous referee for their thorough feedback which significantly improved the presentation of our results. JAP wants to thank Dr. Néstor Espinoza and Mr. Ashok Patel for providing the financial support to visit the Max-Planck-Institut für Astronomie (MPIA), Heidelberg in Germany to perform the present work. A significant part of the present work constitute the final year project work of JAP’s Master’s degree. JAP wants to thank his parent institute – Sardar Vallabhbhai National Institute of Technology, Surat-7, Gujarat, India – and his academic supervisor Prof. K. N. Pathak to give permission to work at MPIA during this period. NE would like to thank M. Günther and T. Daylan for useful discussions regarding uniform analyses of *TESS* known exoplanets.

This research has made use of the NASA Exoplanet Archive, which is operated by the California Institute of Technology, under contract with the National Aeronautics and Space Administration under the Exoplanet Exploration Program.

This research made use of the open source Python package *exotk*, the Exoplanet Characterization Toolkit (Bourque et al. 2021).

APPENDIX

A. DISCREPANT PLANETARY SYSTEMS WITH LITERATURE VALUES

As noted in Section 3.1, our lightcurve analysis showed that for 25 exoplanetary systems, one or more than one of the planetary parameters are at least $3 - \sigma$ away from what is published in the literature. These systems are LTT9779 b, XO-3 b, WASP-161 b, WASP-121 b, HAT-P-2 b, HAT-P-69 b, KELT-11 b, CoRoT-18 b, WASP-4 b, K2-237 b, WASP-131 b, WASP-17 b, KELT-20 b, WASP-31 b, WASP-46 b, WASP-19 b, WASP-92 b, XO-6 b, TOI-157 b, WASP-22 b, K2-260 b, WASP-7 b, WASP-95 b, CoRoT-32 b and HATS-18 b. Here, we perform a more in-depth discussion on what might be producing these offsets on the planetary parameters.

For 11 of those “discrepant” systems (HAT-P-69 b, KELT-11 b, WASP-4 b, WASP-131 b, KELT-20 b, WASP-31 b, WASP-46 b, WASP-22 b, K2-260 b, WASP-95 b and CoRoT-32 b) the offset is in the predicted time-of-transit center versus our computed time-of-transit center, which could either point to possible transit-timing variations (TTVs) in these systems (e.g., WASP-4b is known to have TTVs, which we recover here; see Bourma et al. 2019) or simply act as updates with respect to previous ephemerides which might be outdated. Similar offsets have been found for HAT-P-69 b and WASP-95 b in Shan et al. (2021); however, the timing offsets for KELT-11 b, WASP-131 b, KELT-20 b, WASP-31 b, WASP-46 b, WASP-22 b, K2-260 b and CoRoT-32 b reported here have not been reported elsewhere to our knowledge.

The remaining 14 exoplanetary systems (LTT9779 b, XO-3 b, WASP-161 b, WASP-121 b, HAT-P-2 b, CoRoT-18 b, K2-237 b, WASP-17 b, WASP-19 b, WASP-92 b, XO-6 b, TOI-157 b, WASP-7 b and HATS-18 b) all show planet-to-star radius ratio (R_p/R_*) and/or semi-major axis-to-stellar radius ratio (a/R_*) discrepancies between 3 to 5 sigma from the literature values; some also show time-of-transit center offsets together with those.

From the planetary systems that show discrepancies on a/R_* (5 exoplanetary systems: XO-3 b, HAT-P-2 b, K2-237 b, XO-6 b and TOI-157 b), there are different explanations for the offsets:

- For XO-3 b, while the reported value in this work of $a/R_* = 7.09^{+0.24}_{-0.23}$ is inconsistent with the value in the discovery paper of (Johns-Krull et al. 2008, $a/R_* = 4.95^{+0.18}_{-0.18}$), our value is consistent with that of Wong et al. (2014) of $a/R_* = 7.052^{+0.076}_{-0.097}$. The value in Wong et al. (2014) has much better precision as the orbit is constrained through the entire phase-curve of the exoplanet.
- For HAT-P-2 b, we obtain $a/R_* = 9.04^{+0.19}_{-0.18}$. This value is, in fact, consistent with various values in the literature (Pál et al. 2010; Southworth 2010; Stassun et al. 2017b), including the discovery paper ($a/R_* = 9.770^{+1.100}_{-0.020}$; Bakos et al. 2007). However, it is inconsistent with the value found by Loeillet et al. (2008) of $a/R_* = 10.28^{+0.12}_{-0.19}$. That value, however, was obtained by fitting a radial-velocity only dataset for HAT-P-2 b which includes a measurement of the Rossiter-McLaughlin (RM) effect. Pál et al. (2010) used the same dataset but not considering the radial-velocities obtained in-transit, and considering a wide array of ground-based photometric follow-up transits to obtain their value of $a/R_* = 8.99^{+0.39}_{-0.41}$ which is fully consistent with our solution — this suggests the Loeillet et al. (2008) might be biased given its constrain mainly comes from the RM effect. We consider our parameter here an update to the parameters of this system given these previous attempts.
- K2-237 b was observed by *Kepler/K2* back in 2016, and independant analyses were performed by the teams of Soto et al. (2018, $a/R_* = 5.50^{+0.15}_{-0.11}$) and Smith et al. (2019, $a/R_* = 5.503^{+0.015}_{-0.207}$), both of which give consistent a/R_* values with each other, but inconsistent values at 3-sigma with the ones reported in our present work ($a/R_* = 6.17^{+0.13}_{-0.19}$; see Table 6), especially when compared to the work of Smith et al. (2019). Interestingly, our value of a/R_* is perfectly matched with the recent full re-analysis of the system made by Ikwut-Ukwa et al. (2020, $a/R_* = 6.07^{+0.14}_{-0.18}$). We believe that our offset with the work of Smith et al. (2019) is the product of a simple typo in their upper errorbars (0.015), which are one order of magnitude better than what can be reasonable achieved with the *K2* data-quality; it is interesting, however, that the two analyses made on the (long-cadence) *K2* photometry are systematically lower than the *TESS* short-cadence analyses presented in this work and that of Ikwut-Ukwa et al. (2020).
- For XO-6 b, we also believe our value corresponds to an update with respect to previous constraints on this parameter. First, the value we obtain in our work ($a/R_* = 8.17^{+0.07}_{-0.07}$) is consistent with an independent analysis made on the same *TESS* data by Ridden-Harper et al. (2020, $a/R_* = 8.383 \pm 0.074$). These values are however inconsistent with the one reported in Crouzet et al. (2017) who from the photometry alone conclude on $a/R_* = 9.20 \pm 0.19$, but when combining that data with Doppler tomographic results settle on $a/R_* = 9.08 \pm 0.17$. Interestingly, the constrain on this parameter using only the Doppler tomography in that work is $a/R_* = 8.30^{+1.2}_{-0.8}$, which is fully consistent with the value that both our work and that of Ridden-Harper et al. (2020) retrieve using the *TESS* photometry. It is likely, thus, that the photometric analysis in Crouzet et al. (2017) is somewhat biasing their result towards a larger a/R_* , but it is unclear which part of their analysis could give rise to such a large bias.
- For TOI-157 b, our value for a/R_* of 6.30 ± 0.09 is inconsistent at 3-sigma with that reported in Nielsen et al. (2020) of $5.79^{+0.07}_{-0.07}$. One of the differences between our analyses is that Nielsen et al. (2020) use, along some ground-based photometric follow-up, 8-sectors-worth of 30-min cadence data and 4-sectors-worth of 2-min cadence data, which arguably mostly define the planetary properties. In our analysis, however, we use 12-sectors-worth of 2-minute cadence data. It is interesting to note, in addition, that the differences on this parameter between the Nielsen et al. (2020) estimate and our work go in the same direction as those observed and discussed for K2-237 b before: our analysis obtains a larger value for a/R_* . The only observational similarity between the *TESS* observations of TOI-157 b analyzed by Nielsen et al. (2020) and the *K2* observations of K2-237 b analyzed by the teams of Soto et al. (2018) and Smith et al. (2019) is that both datasets rely heavily on long-cadence data. This is suspiciously consistent with what is expected by morphological lightcurve distortions due

to finite integration time (Kipping 2010): not properly accounting/resampling the lightcurves in long-cadence observations would give rise to smaller values of a/R_* for a fixed period. We suggest, thus, that perhaps the value obtained in Nielsen et al. (2020) is due to the fact that lightcurve resampling following procedures similar to those outlined in Kipping (2010) were either not applied or not performed with sufficient precision to properly account for the effect. Similarly, perhaps this latter option is the case as well for the *K2* observations of K2-237 b analyzed by both Soto et al. (2018) and Smith et al. (2019).

Finally, for the 9 systems that show R_p/R_* discrepancies with literature values (LTT9779 b, WASP-161 b, WASP-121 b, CoRoT-18 b, WASP-17 b, WASP-19 b, WASP-92 b, WASP-7 b and HATS-18 b), different explanations exist:

- For LTT9779 b, we retrieve $R_p/R_* = 0.0337^{+0.0011}_{-0.0009}$, which is inconsistent with the value found by Jenkins et al. (2020) of $R_p/R_* = 0.0455^{+0.0022}_{-0.0017}$. In fact, for this system, our retrieved value for $a/R_* = 7.62^{+0.30}_{-0.36}$ is also significantly discrepant with that of Jenkins et al. (2020, $a/R_* = 3.88 \pm 0.09$). Our retrieved parameter values for this system, however, are most likely wrong and should not be used — we only present them here for completeness and transparency of our process. While the transit fits from both our solutions and the ones reported in Jenkins et al. (2020) both fit the data equally well, the combination of our retrieved a/R_* with the planetary period yield a stellar density of $13342 \pm 1744 \text{ kg/m}^3$ which is completely inconsistent with that obtained through spectroscopy by Jenkins et al. (2020) of $1810 \pm 130 \text{ kg/m}^3$. This two-solution problem was in fact briefly studied by Jenkins et al. (2020) as well in their Methods section.
- For WASP-161 b, we retrieve $R_p/R_* = 0.0751^{+0.0009}_{-0.0008}$, which is much more precise but discrepant at 3-sigma with the one reported by Barkaoui et al. (2019, $R_p/R_* = 0.0671^{+0.0017}_{-0.0017}$). While this target does have a nearby companion about $16''$ to the SE, the PDC algorithm takes this dilution into account on the photometry and as such it is unlikely this is the cause of the discrepancy. The work of Barkaoui et al. (2019) has only one full ground-based transit (with the rest of the follow-up photometry being partial transits) and, as such, we believe our value for R_p/R_* is effectively an update on this parameter. In addition, we also find a discrepant time-of-transit center, which has also been reported by Shan et al. (2021).
- For WASP-121 b, we retrieve $R_p/R_* = 0.1217^{+0.0003}_{-0.0003}$, which is discrepant at about 3-sigma with the value of $R_p/R_* = 0.1245^{+0.0005}_{-0.0005}$ reported in Delrez et al. (2016). Interestingly, the Delrez et al. (2016) value is consistent with analysis of Sector 7 *TESS* data from other teams (see, e.g., Yang et al. 2020; Bourrier et al. 2020; Daylan et al. 2021). In our work, however, we use additional data from Sectors 33 and 34. If we run our analyses on Sector 7 *TESS* data only, our resulting value of $R_p/R_* = 0.12394^{+0.00047}_{-0.00043}$ is consistent with both, the value of Delrez et al. (2016) and the rest of the *TESS* analyses in the literature. However, individual analyses on Sectors 33 and 34 reveal that the transit depth on Sector 7 is significantly larger than the ones observed in those: 500 ppm larger. This might, indeed, be true variability in the transit depth caused either by the star or the planetary atmosphere itself — this has already been suggested by ground-based observations by Wilson et al. (2021). We note that the transit depth reported in this work is consistent with the average transit depth in the HST/WFC3 transit spectrum presented by Evans et al. (2018). We also observe a 3-sigma time-of-transit offset from that of Delrez et al. (2016), which might also hint to possible long-term TTVs.
- For CoRoT-18 b, we obtain $R_p/R_* = 0.1579^{+0.0042}_{-0.0046}$, which is significantly discrepant with the $0.1341^{+0.0019}_{-0.0019}$ value reported in Hébrard et al. (2011). This latter reported value, in turn, agrees well with follow-up ground-based photometry of Southworth (2012). While the discrepant transit depth in the *TESS* photometry could be due to variability either in the star or the planet itself, given the field containing this target is so crowded, it is also possible that the discrepancy in the planet-to-star radius ratio is due to an over-correction of the dilution from nearby sources, similar to the case if WASP-140 b in Section 3.1.
- For WASP-17 b, we retrieve $R_p/R_* = 0.1218^{+0.0016}_{-0.0014}$, which is inconsistent at 3-sigma with the value reported in Anderson et al. (2010, $R_p/R_* = 0.1293^{+0.0008}_{-0.0008}$). We believe, however, that our value is an update on this parameter given the agreement of our value with recent precise HST and Spitzer transit spectroscopy reported by Saba et al. (2021).
- For WASP-19 b, we obtain $R_p/R_* = 0.1519^{+0.0018}_{-0.0020}$, which agrees with some results in the literature, but not with others. In particular, this value agrees with the originally reported value by Hebb et al. (2010) and the

recent *TESS* analysis performed by Wong et al. (2020), but does not with the values reported by Tregloan-Reed et al. (2013), Mancini et al. (2013) and Espinoza et al. (2019b) by more than 3-sigma. This is, in turn, not surprising, given the high levels of stellar activity the star is known to have, which has been observed to directly contaminate the observed transit depths both due to occulted and unocculted spots (see, e.g., Espinoza et al. 2019b).

- For WASP-92 b, we retrieve $R_p/R_* = 0.1068^{+0.0015}_{-0.0022}$, which is inconsistent at 3-sigma with the value reported in Gajdoš et al. (2019) of $R_p/R_* = 0.0963^{+0.0017}_{-0.0017}$. While there seems to be an extended object (the galaxy LEDA 2387340; TIC 10000706526) about 14.8" to the NW of WASP-92, this object is indeed in the TIC catalog, and correctly identified as an extended object in it, which means it is correctly being introduced in the PDC dilution correction. It is, thus, unlikely this is the source of the discrepancy. We believe our value is an update to the one reported in Gajdoš et al. (2019), however, because that work does not have full coverage of the transit event with all their ground-based photometric follow-up. The *TESS* dataset we use here, however, is composed of 3 sectors full of data which comprise a couple of tens of transits in total.
- For WASP-7 b, we obtain $R_p/R_* = 0.0790^{+0.0007}_{-0.0006}$, which is inconsistent at more than 5-sigma from the $R_p/R_* = 0.0956^{+0.0016}_{-0.0016}$ value reported by Southworth et al. (2011). Interestingly, our value is consistent with the discovery paper R_p/R_* reported by Hellier et al. (2009). The larger R_p/R_* reported by Southworth et al. (2011) comes from only one (high-precision) transit, whereas the value reported in this work comes from four high-precision transit events from Sector 27. We would, thus, be tempted to think of our value as the “correct” one. However, it is important to note that the third transit observed by *TESS* shows a possible spot-crossing event feature (see Figure 12), suggesting that perhaps the varying transit depths across different studies is indeed real, and produced by occulted and unocculted stellar heterogeneities such as the ones observed for WASP-19 b.
- Finally, for HATS-18 b, we obtain $R_p/R_* = 0.1456^{+0.0021}_{-0.0024}$, which is inconsistent with the $R_p/R_* = 0.1320^{+0.0004}_{-0.0004}$ value reported in Penev et al. (2016) by more than 5-sigma. This target is quite special because while only observed by *TESS* in Sector 10, its short, 20-hour period implies 26 full transits were used for the analysis presented in this work. All the rest of the parameters are consistent with those of Penev et al. (2016). This target does not have any significant, nearby contaminant — so it is isn’t likely the offset in R_p/R_* is due to miscalculated dilution. The target is, however, active — Penev et al. (2016) measure rotational variability with a period of about 10 days. Our best explanation for this discrepancy, thus, is that the different transit depths could arise due to different levels of stellar activity in the *TESS* observations as compared to those observed by Penev et al. (2016) — i.e., varying transit depths due to both occulted and unocculted spots, similar to the WASP-19 b case. There is evidence, in fact, of varying levels of stellar activity between epochs for HATS-18. While Penev et al. (2016) measure a peak-to-peak amplitude of this variability of order 20 mmag (20,000 ppm) in the HAT-South photometry, we see peak-to-peak amplitudes of this variability in our *TESS* photometry at least 1/3 of that — with a peak-to-peak amplitude of about 6,000 ppm. HATS-18 b transiting brighter regions of the star during the *TESS* observations as compared to the previous transits observed by Penev et al. (2016) could explain, for instance, the larger transit depths observed in our work.

From the above analyses, thus, it seems that 24 out of 25 discrepant systems are really mostly updates to existing reported planetary parameters in the literature for the exoplanets under consideration in this work. Our only real outlier is LTT9799 b. We consider having one confirmed outlier out of a sample of 176 targets is perfectly consistent with random chance and, thus, we consider this a very good check that our procedures are giving consistent (and/or updated) results to previous studies.

B. TABLES

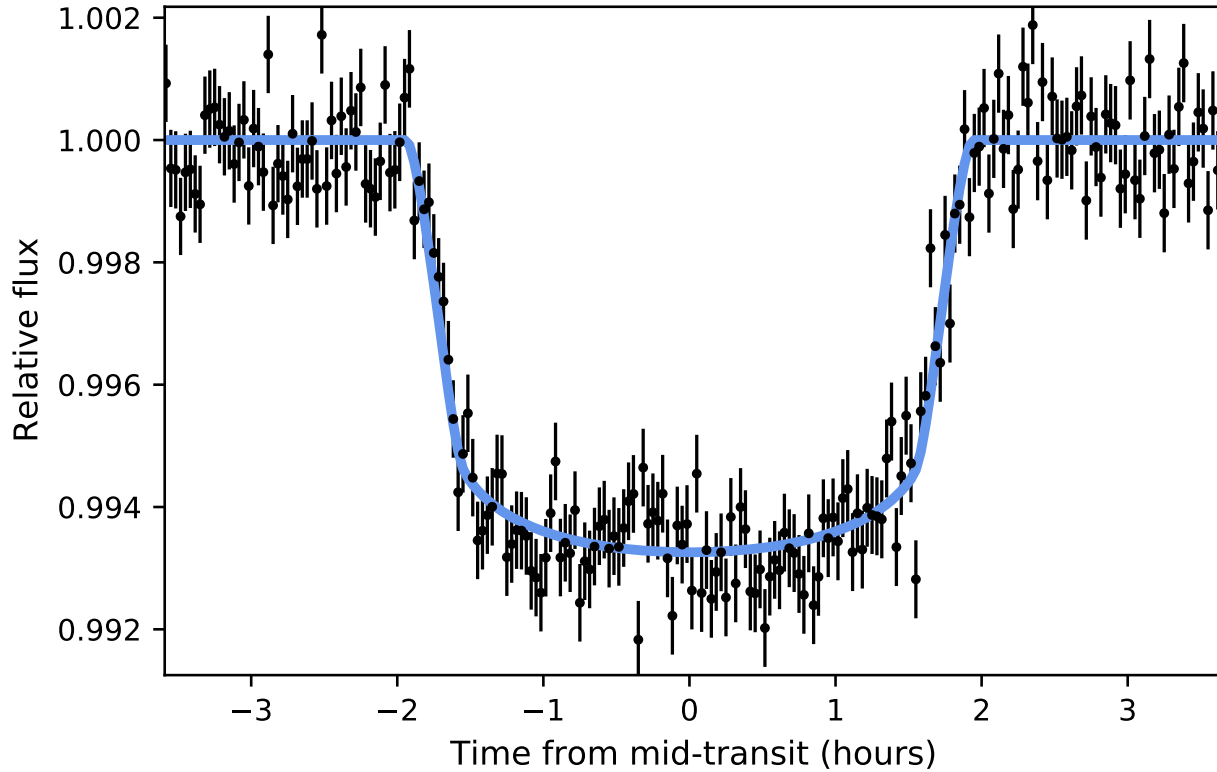


Figure 12. Third transit of WASP-7b observed by *TESS* in Sector 27. An event, suggestive of a spot crossing event, is seen at about 24 minutes before mid-transit.

Table 3. Various stellar properties of our targets. The data was retrieved from the NASA Exoplanet Archive on February 23, 2021. Only first 20 rows are shown here; the full table is available on the website in a machine readable ASCII form.

Star Name	T_{eff} (K)	[M/H]	$\log g$ (cgs)	V_{urb} (km/s)
WASP-61	6250.0	-0.10	4.26	...
WASP-130	5625.0	0.26	4.49	...
HATS-13	5523.0	0.05	4.52	...
WASP-156	4910.0	0.24	4.60	...
NGTS-4	5143.0	-0.28	4.50	...
WASP-190	6400.0	-0.02	4.17	...
WASP-44	5420.0	-0.003	4.49	...
TOI-892	6261.0	0.24	4.26	...
WASP-82	6480.0	0.12	3.96	...
TOI-540	3216.0	0.00	4.44	...

Table 3 continued

Table 3 (*continued*)

Star Name	T_{eff} (K)	[M/H]	$\log g$ (cgs)	V_{turb} (km/s)
WASP-22	6000.0	-0.05	4.50	...
TOI-905	5570.0	0.14	4.50	...
HAT-P-42	5743.0	0.27	4.14	...
WASP-62	6230.0	0.04	4.45	...
HATS-3	6351.0	-0.16	4.22	...
LTT9779	5443.0	0.27	4.35	...
K2-260	6367.0	-0.14	4.15	...
TrES-3	5650.0	-0.20	4.57	...
Qatar-10	6124.0	0.016	4.30	...
WASP-144	5200.0	0.18	4.53	...

Table 4. Limb darkening coefficients calculated using different methods for quadratic law; here EJ15 means the LDCs calculated using the method by Espinoza & Jordán (2015) and C17 implies the tabulated values from Claret (2017), with their *r-method* (C17r) and *q-method* (C17q) when using PHOENIX models * dash indicates that the LDCs for the given target could not be calculated because the effective temperature of the host star is out of the range of Claret (2017) ATLAS tables.

Only first 20 rows are shown here; the full table is available on the website in a machine readable ASCII form.

Star name	u_1	u_2	(EJ15)	u_1	u_2	(EJ15)	u_1	u_2	(EJ15)	u_1^*	u_2^*	(C17)	u_1	u_2	(C17q)	u_1	u_2	(C17q)	u_1	u_2	(C17r)	u_1	u_2	(C17r)	
(Empirical)	(Empirical)	(Empirical)	(EJ15)	(EJ15)	(EJ15)	(EJ15)	(EJ15)	(EJ15)	(EJ15)	(ATLAS)	(ATLAS)	(ATLAS)	(PHOENIX)	(PHOENIX)	(PHOENIX)	(PHOENIX)	(PHOENIX)	(PHOENIX)	(PHOENIX)	(PHOENIX)	(PHOENIX)	(PHOENIX)	(PHOENIX)	(PHOENIX)	
WASP-61	0.26 ^{+0.12} _{-0.13}	0.19 ^{+0.24} _{-0.22}	0.23	0.31	0.30	0.30	0.25	0.25	0.23	0.31	0.31	0.24	0.24	0.38	0.38	0.31	0.31	0.31	0.24	0.24	0.31	0.31	0.31	0.25	0.25
WASP-130	0.25 ^{+0.18} _{-0.16}	0.43 ^{+0.27} _{-0.35}	0.36	0.26	0.36	0.36	0.23	0.23	0.33	0.27	0.27	0.30	0.30	0.34	0.34	0.36	0.36	0.36	0.30	0.30	0.36	0.36	0.36	0.23	0.23
HATS-13	0.31 ^{+0.17} _{-0.17}	0.29 ^{+0.34} _{-0.33}	0.34	0.26	0.37	0.37	0.23	0.23	0.34	0.26	0.26	0.31	0.31	0.33	0.33	0.37	0.37	0.37	0.31	0.31	0.37	0.37	0.37	0.22	0.22
WASP-156	0.52 ^{+0.14} _{-0.15}	0.08 ^{+0.28} _{-0.25}	0.43	0.21	0.44	0.44	0.21	0.21	0.45	0.20	0.20	0.39	0.39	0.30	0.30	0.43	0.43	0.43	0.39	0.39	0.43	0.43	0.43	0.21	0.21
NGTS-4	0.31 ^{+0.35} _{-0.22}	0.10 ^{+0.31} _{-0.24}	0.36	0.25	0.40	0.40	0.21	0.21	0.38	0.23	0.23	0.34	0.34	0.33	0.33	0.40	0.40	0.40	0.34	0.34	0.40	0.40	0.40	0.22	0.22
WASP-190	0.42 ^{+0.20} _{-0.20}	0.30 ^{+0.30} _{-0.32}	0.21	0.32	0.31	0.31	0.24	0.24	0.22	0.32	0.32	0.22	0.22	0.39	0.39	0.30	0.30	0.30	0.22	0.22	0.30	0.30	0.30	0.25	0.25
WASP-44	0.44 ^{+0.21} _{-0.22}	0.30 ^{+0.30} _{-0.37}	0.34	0.26	0.38	0.38	0.23	0.23	0.36	0.25	0.25	0.32	0.32	0.33	0.33	0.38	0.38	0.38	0.32	0.32	0.38	0.38	0.38	0.22	0.22
TOI-892	0.21 ^{+0.12} _{-0.12}	-0.00 ^{+0.17} _{-0.11}	0.24	0.32	0.30	0.30	0.25	0.25	0.24	0.32	0.32	0.24	0.24	0.38	0.38	0.31	0.31	0.31	0.24	0.24	0.31	0.31	0.31	0.25	0.25
WASP-82	0.35 ^{+0.06} _{-0.07}	0.07 ^{+0.12} _{-0.11}	0.21	0.33	0.30	0.30	0.24	0.24	0.21	0.33	0.33	0.20	0.20	0.44	0.44	0.30	0.30	0.30	0.20	0.20	0.30	0.30	0.30	0.24	0.24
TOI-540	0.96 ^{+0.26} _{-0.24}	-0.11 ^{+0.23} _{-0.22}	0.24	0.39	0.14	0.14	0.52	0.52	—	—	—	0.02	0.02	0.72	0.72	0.12	0.12	0.12	0.02	0.02	0.12	0.12	0.12	0.53	0.53
WASP-22	0.19 ^{+0.11} _{-0.11}	0.30 ^{+0.21} _{-0.21}	0.26	0.30	0.32	0.32	0.25	0.25	0.26	0.30	0.30	0.26	0.26	0.36	0.36	0.32	0.32	0.32	0.26	0.26	0.32	0.32	0.32	0.25	0.25
TOI-905	0.59 ^{+0.38} _{-0.37}	0.19 ^{+0.41} _{-0.44}	0.34	0.26	0.36	0.36	0.23	0.23	0.34	0.27	0.27	0.31	0.31	0.33	0.33	0.37	0.37	0.37	0.31	0.31	0.37	0.37	0.37	0.22	0.22
HAT-P-42	0.25 ^{+0.17} _{-0.15}	0.39 ^{+0.29} _{-0.31}	0.31	0.29	0.35	0.35	0.24	0.24	0.31	0.28	0.28	0.27	0.27	0.39	0.39	0.34	0.34	0.34	0.27	0.27	0.34	0.34	0.34	0.24	0.24
WASP-62	0.30 ^{+0.01} _{-0.01}	0.13 ^{+0.03} _{-0.03}	0.24	0.31	0.30	0.30	0.25	0.25	0.24	0.31	0.31	0.24	0.24	0.37	0.37	0.31	0.31	0.31	0.24	0.24	0.31	0.31	0.31	0.25	0.25
HATS-3	0.22 ^{+0.15} _{-0.13}	0.20 ^{+0.24} _{-0.24}	0.23	0.31	0.31	0.31	0.24	0.24	0.22	0.31	0.31	0.23	0.23	0.39	0.39	0.31	0.31	0.31	0.23	0.23	0.31	0.31	0.31	0.24	0.24
LTT9779	1.35 ^{+0.10} _{-0.11}	-0.41 ^{+0.12} _{-0.13}	0.36	0.26	0.38	0.38	0.23	0.23	0.36	0.25	0.25	0.31	0.31	0.35	0.35	0.37	0.37	0.37	0.31	0.31	0.37	0.37	0.37	0.23	0.23
K2-260	0.29 ^{+0.15} _{-0.16}	0.14 ^{+0.31} _{-0.23}	0.23	0.31	0.31	0.31	0.24	0.24	0.22	0.31	0.31	0.23	0.23	0.39	0.39	0.31	0.31	0.31	0.23	0.23	0.31	0.31	0.31	0.24	0.24
TrES-3	0.45 ^{+0.41} _{-0.30}	0.11 ^{+0.35} _{-0.33}	0.29	0.29	0.36	0.36	0.23	0.23	0.31	0.28	0.28	0.30	0.30	0.33	0.33	0.36	0.36	0.36	0.30	0.30	0.36	0.36	0.36	0.23	0.23
Qatar-10	0.15 ^{+0.10} _{-0.08}	0.55 ^{+0.20} _{-0.22}	0.27	0.30	0.31	0.31	0.25	0.25	0.25	0.31	0.31	0.25	0.25	0.38	0.38	0.32	0.32	0.32	0.25	0.25	0.32	0.32	0.32	0.25	0.25
WASP-144	0.26 ^{+0.23} _{-0.17}	0.29 ^{+0.34} _{-0.32}	0.39	0.23	0.40	0.40	0.22	0.22	0.40	0.23	0.23	0.34	0.34	0.32	0.32	0.40	0.40	0.40	0.34	0.34	0.40	0.40	0.40	0.22	0.22

Table 5. SPAM limb darkening coefficients calculated using different methods for quadratic law; here EJ15 means the LDCs calculated using the method by Espinoza & Jordán (2015) and C17 implies the tabulated values from Claret (2017), with their *r-method* (C17r) and *q-method* (C17q) when using PHOENIX models.

Only first 20 rows are shown here; the full table is available on the website in a machine readable ASCII form.

Star name	u_1	u_2	u_1	u_2	u_1	u_2	u_1	u_2	u_1	u_2
	(EJ15	(EJ15	(EJ15	(EJ15	(C17	(C17	(C17q	(C17q	(C17r	(C17r
	ATLAS)	ATLAS)	PHOENIX)	PHOENIX)	ATLAS)	ATLAS)	PHOENIX)	PHOENIX)	PHOENIX)	PHOENIX)
WASP-61	0.30	0.20	0.35	0.17	0.30	0.20	0.37	0.16	0.37	0.15
WASP-130	0.40	0.19	0.42	0.14	0.37	0.20	0.40	0.16	0.41	0.14
HATS-13	0.38	0.18	0.42	0.14	0.38	0.19	0.42	0.15	0.42	0.14
WASP-156	0.48	0.13	0.50	0.11	0.50	0.11	0.49	0.12	0.49	0.11
NGTS-4	0.31	0.35	0.32	0.35	0.32	0.35	0.32	0.36	0.32	0.35
WASP-190	0.21	0.29	0.24	0.31	0.21	0.29	0.25	0.32	0.24	0.31
WASP-44	0.38	0.20	0.43	0.14	0.38	0.20	0.42	0.16	0.42	0.14
TOI-892	0.23	0.31	0.24	0.32	0.23	0.31	0.25	0.32	0.37	0.15
WASP-82	0.21	0.32	0.37	0.14	0.21	0.32	0.36	0.17	0.37	0.14
TOI-540	0.25	0.36	0.22	0.35	-0.04	0.20	0.21	0.34	0.21	0.34
WASP-22	0.31	0.21	0.37	0.16	0.32	0.21	0.37	0.17	0.37	0.16
TOI-905	0.37	0.21	0.41	0.14	0.36	0.21	0.39	0.18	0.41	0.15
HAT-P-42	0.26	0.32	0.41	0.14	0.26	0.32	0.38	0.18	0.41	0.14
WASP-62	0.29	0.22	0.36	0.16	0.29	0.21	0.35	0.18	0.36	0.16
HATS-3	0.22	0.29	0.38	0.14	0.21	0.29	0.35	0.18	0.37	0.15
LTT9779	0.28	0.34	0.28	0.34	0.28	0.34	0.28	0.34	0.28	0.33
K2-260	0.29	0.21	0.37	0.14	0.28	0.21	0.36	0.16	0.36	0.15
TrES-3	0.31	0.24	0.41	0.15	0.33	0.23	0.38	0.19	0.40	0.16
Qatar-10	0.31	0.22	0.37	0.16	0.30	0.22	0.37	0.17	0.37	0.15
WASP-144	0.43	0.16	0.46	0.13	0.44	0.16	0.44	0.15	0.45	0.13

Table 6. Retrieved planetary parameters along with their literature values. The data of literature planetary parameters was extracted from the NASA Exoplanet Archive on February 23, 2021.

Only first 20 rows are shown here; the full table is available on the website in a machine readable ASCII form.

Planet name	R_p/R_*	a/R_*	$t_c - 2458000$	R_p/R_*	a/R_*	$t_c - 2458000$
	(This work)	(This work)	(This work)	(Literature)	(Literature)	(Literature)
WASP-61b	$0.0934^{+0.0008}_{-0.0009}$	$8.09^{+0.11}_{-0.24}$	$1198.73545^{+0.00033}_{-0.00034}$	$0.0937^{+0.0031}_{-0.0031}$	$8.15^{+0.24}_{-0.24}$	1198.738 ± 0.003
WASP-130b	$0.0955^{+0.0025}_{-0.0021}$	$24.15^{+1.42}_{-1.62}$	$607.58558^{+0.00042}_{-0.00041}$	$0.0955^{+0.0044}_{-0.0044}$	$22.67^{+0.77}_{-0.77}$	607.586 ± 0.001
HATS-13b	$0.1427^{+0.0033}_{-0.0028}$	$9.76^{+0.30}_{-0.51}$	$1083.00912^{+0.00053}_{-0.00053}$	$0.1402^{+0.0016}_{-0.0016}$	$9.82^{+0.18}_{-0.18}$	1083.006 ± 0.002
WASP-156b	$0.0672^{+0.0009}_{-0.0008}$	$12.86^{+0.23}_{-0.47}$	$1169.86001^{+0.00030}_{-0.00028}$	$0.0685^{+0.0012}_{-0.0012}$	$12.80^{+0.30}_{-0.30}$	1169.861 ± 0.004
NGTS-4b	$0.0341^{+0.0017}_{-0.0018}$	$5.69^{+0.45}_{-1.01}$	$1227.52707^{+0.00111}_{-0.00098}$	$0.0350^{+0.0030}_{-0.0030}$	$4.79^{+1.21}_{-1.21}$	1227.529 ± 0.010

Table 6 continued

Table 6 (continued)

Planet name	R_p/R_*	a/R_*	$t_c - 2458000$	R_p/R_*	a/R_*	$t_c - 2458000$
	(This work)	(This work)	(This work)	(Literature)	(Literature)	(Literature)
WASP-190b	$0.0781^{+0.0029}_{-0.0020}$	$9.05^{+0.68}_{-0.88}$	$1098.12518^{+0.00064}_{-0.00065}$	$0.0741^{+0.0075}_{-0.0075}$	$8.95^{+0.57}_{-0.57}$	1098.122 ± 0.001
WASP-44b	$0.1174^{+0.0040}_{-0.0036}$	$8.47^{+0.67}_{-0.70}$	$393.84978^{+0.00035}_{-0.00036}$	$0.1248^{+0.0023}_{-0.0023}$	$8.20^{+0.43}_{-0.43}$	393.8498 ± 0.0004
TOI-892b	$0.0800^{+0.0009}_{-0.0009}$	$15.77^{+0.27}_{-0.64}$	$1208.92591^{+0.00064}_{-0.00062}$	$0.0790^{+0.0010}_{-0.0010}$	$14.20^{+0.80}_{-0.80}$	1208.922 ± 0.005
WASP-82b	$0.0773^{+0.0004}_{-0.0004}$	$4.42^{+0.04}_{-0.07}$	$449.78954^{+0.00017}_{-0.00016}$	$0.0788^{+0.0037}_{-0.0037}$	$4.43^{+0.15}_{-0.15}$	449.794 ± 0.002
TOI-540b	$0.0462^{+0.0028}_{-0.0051}$	$13.31^{+4.68}_{-2.43}$	$1199.92424^{+0.00030}_{-0.00029}$	$0.0436^{+0.0012}_{-0.0012}$	$13.90^{+0.72}_{-0.72}$	1199.925 ± 0.001
WASP-22b	$0.1001^{+0.0011}_{-0.0011}$	$8.28^{+0.22}_{-0.30}$	$422.50014^{+0.00023}_{-0.00023}$	$0.0978^{+0.0012}_{-0.0012}$	$8.94^{+0.85}_{-0.85}$	422.468 ± 0.008
TOI-905b	$0.1296^{+0.0027}_{-0.0024}$	$11.47^{+0.42}_{-0.40}$	$639.56977^{+0.00021}_{-0.00021}$	$0.1312^{+0.0079}_{-0.0079}$	$10.94^{+0.50}_{-0.50}$	639.5695 ± 0.0002
HAT-P-42b	$0.0811^{+0.0013}_{-0.0012}$	$9.75^{+0.23}_{-0.48}$	$1252.87532^{+0.00052}_{-0.00052}$	$0.0860^{+0.0033}_{-0.0033}$	$8.08^{+0.82}_{-0.82}$	1252.901 ± 0.023
WASP-62b	$0.1111^{+0.0001}_{-0.0001}$	$9.72^{+0.03}_{-0.03}$	$1252.58570^{+0.00004}_{-0.00004}$	$0.1105^{+0.0003}_{-0.0003}$	$9.55^{+0.41}_{-0.41}$	1252.594 ± 0.002
HATS-3b	$0.0973^{+0.0011}_{-0.0012}$	$8.01^{+0.34}_{-0.34}$	$337.89608^{+0.00031}_{-0.00031}$	$0.1011^{+0.0006}_{-0.0006}$	$7.42^{+0.12}_{-0.12}$	337.896 ± 0.003
LTT9779b	$0.0337^{+0.0011}_{-0.0009}$	$7.62^{+0.30}_{-0.36}$	$1112.22021^{+0.00017}_{-0.00017}$	$0.0455^{+0.0022}_{-0.0022}$	$3.88^{+0.09}_{-0.09}$	1112.208 ± 0.009
K2-260b	$0.0947^{+0.0016}_{-0.0017}$	$5.11^{+0.11}_{-0.20}$	$1186.61999^{+0.00056}_{-0.00057}$	$0.0973^{+0.0003}_{-0.0003}$	$5.29^{+0.03}_{-0.03}$	1186.604 ± 0.001
TrES-3b	$0.1706^{+0.0058}_{-0.0039}$	$5.82^{+0.12}_{-0.13}$	$1034.47459^{+0.00009}_{-0.00009}$	$0.1660^{+0.0024}_{-0.0024}$	$5.95^{+0.05}_{-0.05}$	1034.472 ± 0.001
Qatar-10b	$0.1255^{+0.0015}_{-0.0015}$	$5.05^{+0.08}_{-0.12}$	$1034.37308^{+0.00021}_{-0.00020}$	$0.1265^{+0.0010}_{-0.0010}$	$4.90^{+0.12}_{-0.12}$	1034.371 ± 0.005
WASP-144b	$0.1128^{+0.0029}_{-0.0041}$	$7.32^{+0.73}_{-0.60}$	$1071.05883^{+0.00038}_{-0.00037}$	$0.1079^{+0.0013}_{-0.0013}$	$8.39^{+0.23}_{-0.23}$	1071.060 ± 0.001

C. FIGURES

REFERENCES

- Anderson, D. R., Hellier, C., Gillon, M., et al. 2010, ApJ, 709, 159, doi: [10.1088/0004-637X/709/1/159](https://doi.org/10.1088/0004-637X/709/1/159)
- Bakos, G. Á., Kovács, G., Torres, G., et al. 2007, ApJ, 670, 826, doi: [10.1086/521866](https://doi.org/10.1086/521866)
- Barkaoui, K., Burdanov, A., Hellier, C., et al. 2019, AJ, 157, 43, doi: [10.3847/1538-3881/aaf422](https://doi.org/10.3847/1538-3881/aaf422)
- Bonomo, A. S., Desidera, S., Benatti, S., et al. 2017, A&A, 602, A107, doi: [10.1051/0004-6361/201629882](https://doi.org/10.1051/0004-6361/201629882)
- Bouma, L. G., Winn, J. N., Baxter, C., et al. 2019, AJ, 157, 217, doi: [10.3847/1538-3881/ab189f](https://doi.org/10.3847/1538-3881/ab189f)
- Bourque, M., Espinoza, N., Filippazzo, J., et al. 2021, The Exoplanet Characterization Toolkit (ExoCTK), 1.0.0, Zenodo, doi: [10.5281/zenodo.4556063](https://doi.org/10.5281/zenodo.4556063)
- Bourrier, V., Ehrenreich, D., Lendl, M., et al. 2020, A&A, 635, A205, doi: [10.1051/0004-6361/201936640](https://doi.org/10.1051/0004-6361/201936640)
- Buchner, J., Georgakakis, A., Nandra, K., et al. 2014, A&A, 564, A125, doi: [10.1051/0004-6361/201322971](https://doi.org/10.1051/0004-6361/201322971)
- Castelli, F., & Kurucz, R. L. 2003, in IAU Symposium, Vol. 210, Modelling of Stellar Atmospheres, ed. N. Piskunov, W. W. Weiss, & D. F. Gray, A20. <https://arxiv.org/abs/astro-ph/0405087>
- Claret, A. 2000, A&A, 363, 1081
- . 2017, A&A, 600, A30, doi: [10.1051/0004-6361/201629705](https://doi.org/10.1051/0004-6361/201629705)
- Claret, A., & Hauschildt, P. H. 2003, A&A, 412, 241, doi: [10.1051/0004-6361:20031405](https://doi.org/10.1051/0004-6361:20031405)
- Claret, A., Hauschildt, P. H., & Witte, S. 2012, A&A, 546, A14, doi: [10.1051/0004-6361/201219849](https://doi.org/10.1051/0004-6361/201219849)
- Crouzet, N., McCullough, P. R., Long, D., et al. 2017, AJ, 153, 94, doi: [10.3847/1538-3881/153/3/94](https://doi.org/10.3847/1538-3881/153/3/94)
- Csizmadia, S., Pasternacki, T., Dreyer, C., et al. 2013, A&A, 549, A9, doi: [10.1051/0004-6361/201219888](https://doi.org/10.1051/0004-6361/201219888)
- Daylan, T., Günther, M. N., Mikal-Evans, T., et al. 2021, AJ, 161, 131, doi: [10.3847/1538-3881/abd8d2](https://doi.org/10.3847/1538-3881/abd8d2)
- Delrez, L., Santerne, A., Almenara, J. M., et al. 2016, MNRAS, 458, 4025, doi: [10.1093/mnras/stw522](https://doi.org/10.1093/mnras/stw522)
- Diaz-Cordoves, J., & Gimenez, A. 1992, A&A, 259, 227
- Espinoza, N., & Jordán, A. 2015, MNRAS, 450, 1879, doi: [10.1093/mnras/stv744](https://doi.org/10.1093/mnras/stv744)
- . 2016, MNRAS, 457, 3573, doi: [10.1093/mnras/stw224](https://doi.org/10.1093/mnras/stw224)
- Espinoza, N., Kossakowski, D., & Brahm, R. 2019a, MNRAS, 490, 2262, doi: [10.1093/mnras/stz2688](https://doi.org/10.1093/mnras/stz2688)
- Espinoza, N., Rackham, B. V., Jordán, A., et al. 2019b, MNRAS, 482, 2065, doi: [10.1093/mnras/sty2691](https://doi.org/10.1093/mnras/sty2691)
- Evans, T. M., Sing, D. K., Goyal, J. M., et al. 2018, AJ, 156, 283, doi: [10.3847/1538-3881/aabeff](https://doi.org/10.3847/1538-3881/aabeff)
- Feroz, F., Hobson, M. P., & Bridges, M. 2009, MNRAS, 398, 1601, doi: [10.1111/j.1365-2966.2009.14548.x](https://doi.org/10.1111/j.1365-2966.2009.14548.x)

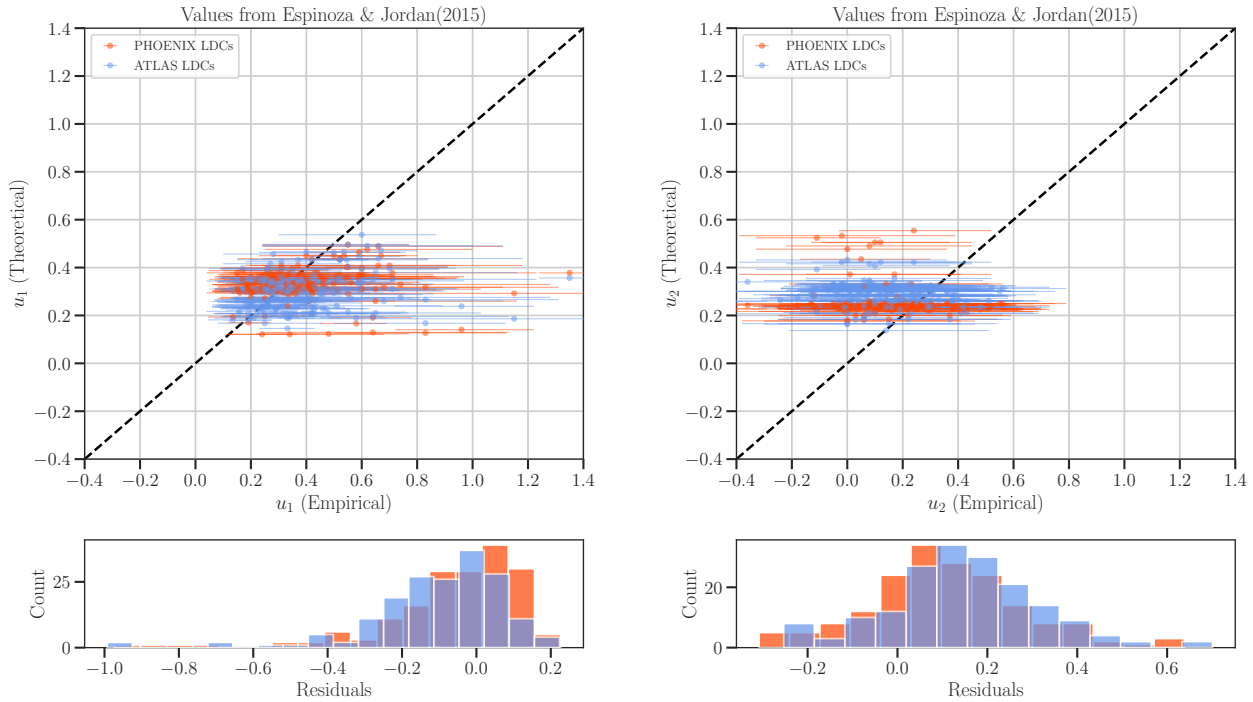


Figure 13. Comparison of the retrieved LDCs u_1 and u_2 from the TESS data with the one calculated from the model stellar atmospheres using the code provided by Espinoza & Jordán (2015). In upper panel, y-axis represents the theoretical LDCs while x-axis shows the empirical values of LDCs. The black dashed line is the line of equality between the x- and y- axis. On the other hand, the lower panel shows the distribution of residuals between the theoretical and empirical LDCs.

Foreman-Mackey, D., Agol, E., Ambikasaran, S., & Angus, R. 2017, *AJ*, 154, 220, doi: [10.3847/1538-3881/aa9332](https://doi.org/10.3847/1538-3881/aa9332)

Gajdoš, P., Vaňko, M., Jakubík, M., et al. 2019, *MNRAS*, 485, 3580, doi: [10.1093/mnras/stz676](https://doi.org/10.1093/mnras/stz676)

Hayek, W., Sing, D., Pont, F., & Asplund, M. 2012, *A&A*, 539, A102, doi: [10.1051/0004-6361/201117868](https://doi.org/10.1051/0004-6361/201117868)

Hebb, L., Collier-Cameron, A., Triaud, A. H. M. J., et al. 2010, *ApJ*, 708, 224, doi: [10.1088/0004-637X/708/1/224](https://doi.org/10.1088/0004-637X/708/1/224)

Hébrard, G., Evans, T. M., Alonso, R., et al. 2011, *A&A*, 533, A130, doi: [10.1051/0004-6361/201117192](https://doi.org/10.1051/0004-6361/201117192)

Hellier, C., Anderson, D. R., Gillon, M., et al. 2009, *ApJL*, 690, L89, doi: [10.1088/0004-637X/690/1/L89](https://doi.org/10.1088/0004-637X/690/1/L89)

Hellier, C., Anderson, D. R., Cameron, A. C., et al. 2017, *MNRAS*, 465, 3693, doi: [10.1093/mnras/stw3005](https://doi.org/10.1093/mnras/stw3005)

Howarth, I. D. 2011, *MNRAS*, 418, 1165, doi: [10.1111/j.1365-2966.2011.19568.x](https://doi.org/10.1111/j.1365-2966.2011.19568.x)

Husser, T. O., Wende-von Berg, S., Dreizler, S., et al. 2013, *A&A*, 553, A6, doi: [10.1051/0004-6361/201219058](https://doi.org/10.1051/0004-6361/201219058)

Ikwut-Ukwa, M., Rodriguez, J. E., Bieryla, A., et al. 2020, *AJ*, 160, 209, doi: [10.3847/1538-3881/aba964](https://doi.org/10.3847/1538-3881/aba964)

Jenkins, J. S., Díaz, M. R., Kurtovic, N. T., et al. 2020, *Nature Astronomy*, 4, 1148, doi: [10.1038/s41550-020-1142-z](https://doi.org/10.1038/s41550-020-1142-z)

Johns-Krull, C. M., McCullough, P. R., Burke, C. J., et al. 2008, *ApJ*, 677, 657, doi: [10.1086/528950](https://doi.org/10.1086/528950)

Kipping, D. M. 2010, *MNRAS*, 408, 1758, doi: [10.1111/j.1365-2966.2010.17242.x](https://doi.org/10.1111/j.1365-2966.2010.17242.x)

—. 2013, *MNRAS*, 435, 2152, doi: [10.1093/mnras/stt1435](https://doi.org/10.1093/mnras/stt1435)

Klinglesmith, D. A., & Sobieski, S. 1970, *AJ*, 75, 175, doi: [10.1086/110960](https://doi.org/10.1086/110960)

Kopal, Z. 1950, *Harvard College Observatory Circular*, 454, 1

Kreidberg, L. 2015, *PASP*, 127, 1161, doi: [10.1086/683602](https://doi.org/10.1086/683602)

—. 2018, *Exoplanet Atmosphere Measurements from Transmission Spectroscopy and Other Planet Star Combined Light Observations* (Springer International Publishing), 100, doi: [10.1007/978-3-319-55333-7_100](https://doi.org/10.1007/978-3-319-55333-7_100)

Loeillet, B., Shporer, A., Bouchy, F., et al. 2008, *A&A*, 481, 529, doi: [10.1051/0004-6361:20078167](https://doi.org/10.1051/0004-6361:20078167)

Maciejewski, G. 2020, *AcA*, 70, 181, doi: [10.32023/0001-5237/70.3.2](https://doi.org/10.32023/0001-5237/70.3.2)

Mancini, L., Ciceri, S., Chen, G., et al. 2013, *MNRAS*, 436, 2, doi: [10.1093/mnras/stt1394](https://doi.org/10.1093/mnras/stt1394)

Mandel, K., & Agol, E. 2002, *ApJL*, 580, L171, doi: [10.1086/345520](https://doi.org/10.1086/345520)

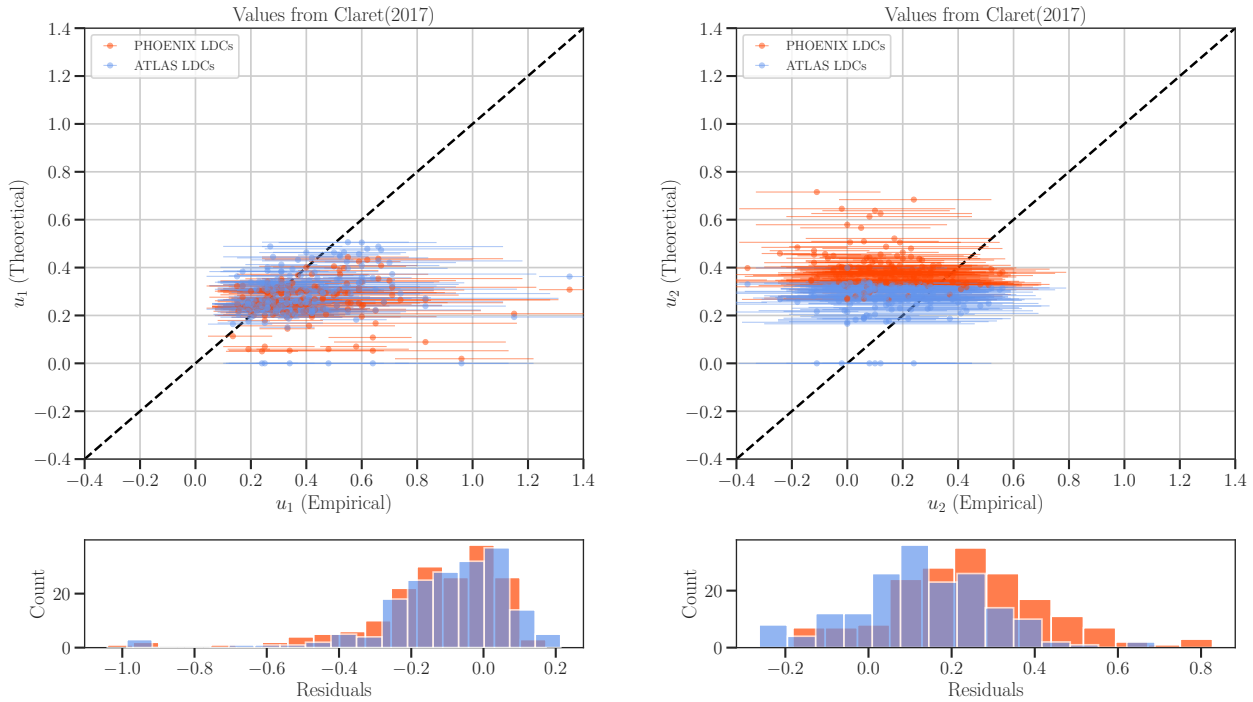


Figure 14. Comparison of the retrieved u_1 from the TESS data with the one calculated from the model stellar atmospheres using the tabulated values from Claret (2017). In upper panel, y-axis represents the theoretical LDCs while x-axis shows the empirical values of LDCs. The black dashed line is the line of equality between the x- and y- axis. On the other hand, the lower panel shows the distribution of residuals between the theoretical and empirical LDCs.

Maxted, P. F. L. 2018, *A&A*, 616, A39,
doi: [10.1051/0004-6361/201832944](https://doi.org/10.1051/0004-6361/201832944)

Morello, G., Tsiaras, A., Howarth, I. D., & Homeier, D. 2017, *AJ*, 154, 111, doi: [10.3847/1538-3881/aa8405](https://doi.org/10.3847/1538-3881/aa8405)

Müller, H. M., Huber, K. F., Czesla, S., Wolter, U., & Schmitt, J. H. M. M. 2013a, *A&A*, 560, A112,
doi: [10.1051/0004-6361/201322079](https://doi.org/10.1051/0004-6361/201322079)

—. 2013b, *A&A*, 560, A112,
doi: [10.1051/0004-6361/201322079](https://doi.org/10.1051/0004-6361/201322079)

Neilson, H. R., McNeil, J. T., Ignace, R., & Lester, J. B. 2017, *ApJ*, 845, 65, doi: [10.3847/1538-4357/aa7edf](https://doi.org/10.3847/1538-4357/aa7edf)

Nielsen, L. D., Brahm, R., Bouchy, F., et al. 2020, *A&A*, 639, A76, doi: [10.1051/0004-6361/202037941](https://doi.org/10.1051/0004-6361/202037941)

Pál, A., Bakos, G. Á., Torres, G., et al. 2010, *MNRAS*, 401, 2665, doi: [10.1111/j.1365-2966.2009.15849.x](https://doi.org/10.1111/j.1365-2966.2009.15849.x)

Penev, K., Hartman, J. D., Bakos, G. Á., et al. 2016, *AJ*, 152, 127, doi: [10.3847/0004-6256/152/5/127](https://doi.org/10.3847/0004-6256/152/5/127)

Ricker, G. R., Winn, J. N., Vanderspek, R., et al. 2014, *Journal of Astronomical Telescopes, Instruments, and Systems*, 1, 1, doi: [10.1117/1.JATIS.1.1.014003](https://doi.org/10.1117/1.JATIS.1.1.014003)

Ridden-Harper, A., Turner, J. D., & Jayawardhana, R. 2020, *AJ*, 160, 249, doi: [10.3847/1538-3881/abba1e](https://doi.org/10.3847/1538-3881/abba1e)

Saba, A., Tsiaras, A., Morvan, M., et al. 2021, arXiv e-prints, arXiv:2108.13721.

<https://arxiv.org/abs/2108.13721>

Sandford, E., & Kipping, D. 2017, *AJ*, 154, 228,
doi: [10.3847/1538-3881/aa94bf](https://doi.org/10.3847/1538-3881/aa94bf)

Schwarz, G. 1978, *Ann. Statist.*, 6, 461,
doi: [10.1214/aos/1176344136](https://doi.org/10.1214/aos/1176344136)

Schwarzschild, K. 1906, *Nachrichten von der Königlichen Gesellschaft der Wissenschaften zu Göttingen. Math.-phys. Klasse*, 195, 41

Seager, S., & Mallén-Ornelas, G. 2003, *ApJ*, 585, 1038,
doi: [10.1086/346105](https://doi.org/10.1086/346105)

Shan, S.-S., Yang, F., Lu, Y.-J., et al. 2021, arXiv e-prints, arXiv:2111.06678. <https://arxiv.org/abs/2111.06678>

Sing, D. K., Désert, J. M., Lecavelier Des Etangs, A., et al. 2009, *A&A*, 505, 891, doi: [10.1051/0004-6361/200912776](https://doi.org/10.1051/0004-6361/200912776)

Smith, A. M. S., Csizmadia, S., Gandolfi, D., et al. 2019, *AcA*, 69, 135, doi: [10.32023/0001-5237/69.2.3](https://doi.org/10.32023/0001-5237/69.2.3)

Soto, M. G., Díaz, M. R., Jenkins, J. S., et al. 2018, *MNRAS*, 478, 5356, doi: [10.1093/mnras/sty1334](https://doi.org/10.1093/mnras/sty1334)

Southworth, J. 2008, *MNRAS*, 386, 1644,
doi: [10.1111/j.1365-2966.2008.13145.x](https://doi.org/10.1111/j.1365-2966.2008.13145.x)

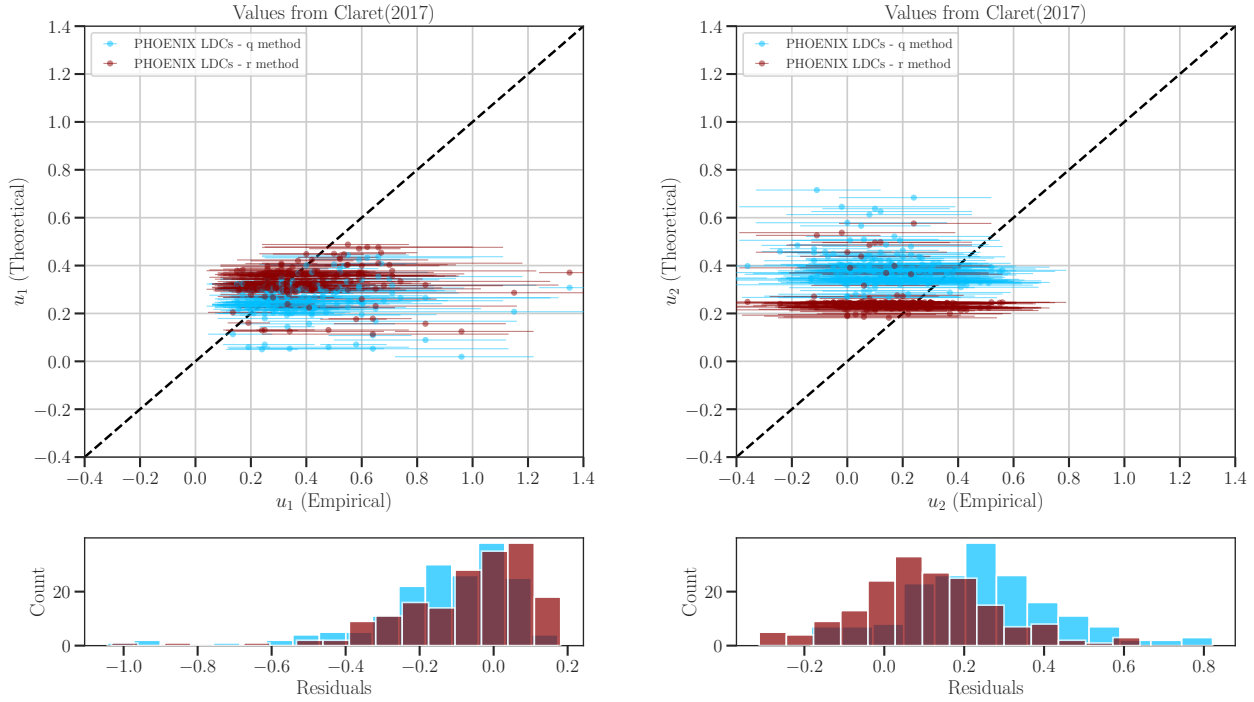


Figure 15. Comparison of the retrieved u_1 and u_2 coefficients from the TESS data with the one calculated from the model stellar atmospheres using tabulated values from Claret (2017) using *r-method* and *q-method*.

—. 2010, MNRAS, 408, 1689,

doi: [10.1111/j.1365-2966.2010.17231.x](https://doi.org/10.1111/j.1365-2966.2010.17231.x)

—. 2012, MNRAS, 426, 1291,

doi: [10.1111/j.1365-2966.2012.21756.x](https://doi.org/10.1111/j.1365-2966.2012.21756.x)

Southworth, J., Dominik, M., Jørgensen, U. G., et al. 2011, A&A, 527, A8, doi: [10.1051/0004-6361/201016183](https://doi.org/10.1051/0004-6361/201016183)

Speagle, J. S. 2020, MNRAS, 493, 3132,

doi: [10.1093/mnras/staa278](https://doi.org/10.1093/mnras/staa278)

Stassun, K. G., Collins, K. A., & Gaudi, B. S. 2017a, AJ, 153, 136, doi: [10.3847/1538-3881/aa5df3](https://doi.org/10.3847/1538-3881/aa5df3)

—. 2017b, AJ, 153, 136, doi: [10.3847/1538-3881/aa5df3](https://doi.org/10.3847/1538-3881/aa5df3)

Tregloan-Reed, J., Southworth, J., & Tappert, C. 2013, MNRAS, 428, 3671, doi: [10.1093/mnras/sts306](https://doi.org/10.1093/mnras/sts306)

Wilson, J., Gibson, N. P., Lothringer, J. D., et al. 2021, MNRAS, 503, 4787, doi: [10.1093/mnras/stab797](https://doi.org/10.1093/mnras/stab797)

Wittkowski, M., Aufdenberg, J. P., & Kervella, P. 2004, A&A, 413, 711, doi: [10.1051/0004-6361:20034149](https://doi.org/10.1051/0004-6361:20034149)

Wong, I., Knutson, H. A., Cowan, N. B., et al. 2014, ApJ, 794, 134, doi: [10.1088/0004-637X/794/2/134](https://doi.org/10.1088/0004-637X/794/2/134)

Wong, I., Benneke, B., Shporer, A., et al. 2020, AJ, 159, 104, doi: [10.3847/1538-3881/ab6d6e](https://doi.org/10.3847/1538-3881/ab6d6e)

Yang, F., Chary, R.-R., & Liu, J.-F. 2020, arXiv e-prints, arXiv:2012.08744. <https://arxiv.org/abs/2012.08744>

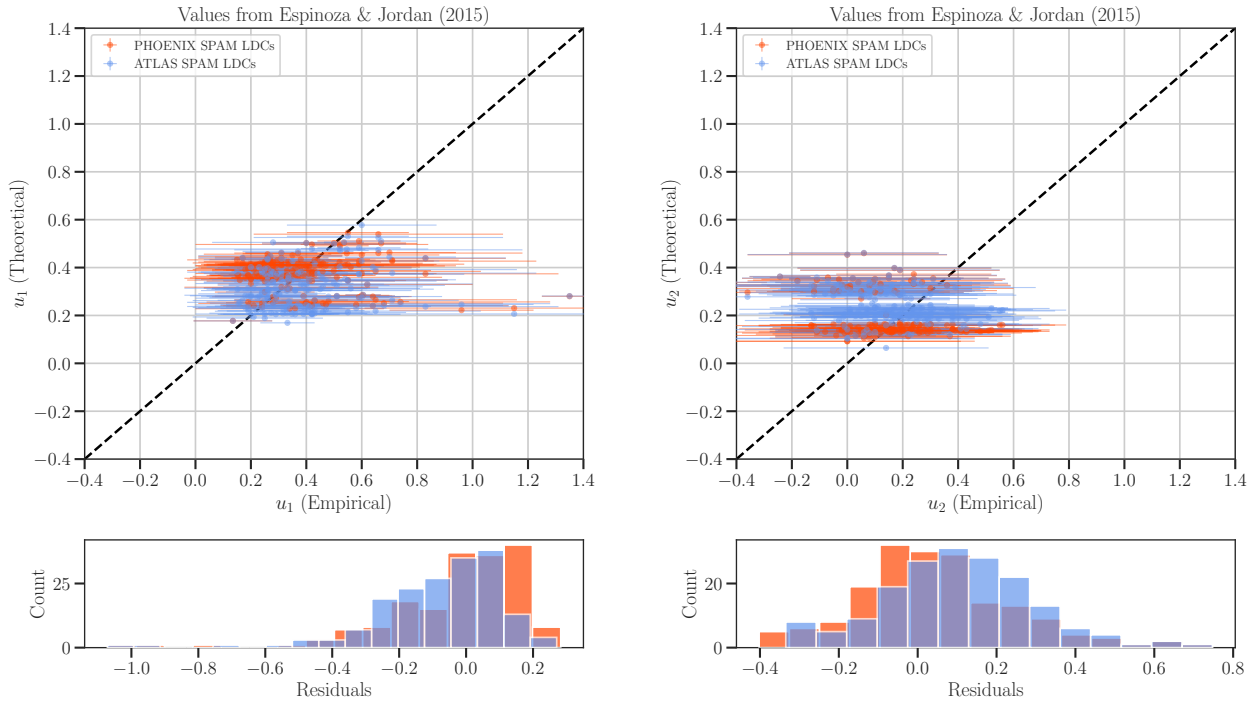


Figure 16. Comparison of the retrieved LDCs u_1 and u_2 from the TESS data with the SPAM LDCs. The later made use of non-linear LDCs from the code provided by [Espinoza & Jordán \(2015\)](#). In upper panel, y-axis represents the SPAM LDCs while x-axis shows the empirical values of LDCs. The black dashed line is the line of equality between the x- and y- axis. On the other hand, the lower panel shows the distribution of residuals between the SPAM and empirical LDCs.

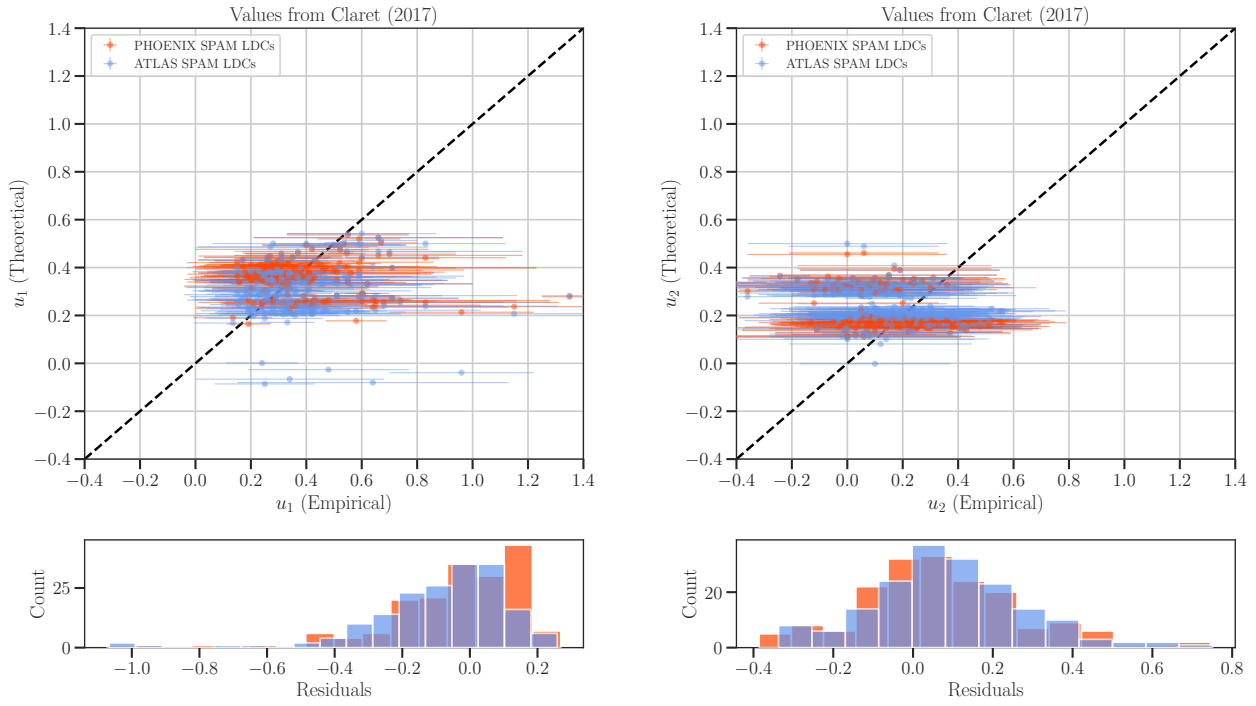


Figure 17. Comparison of the retrieved LDCs u_1 and u_2 from the TESS data with the SPAM LDCs. The later made use of non-linear LDCs from the code provided by Claret (2017). In upper panel, y-axis represents the SPAM LDCs while x-axis shows the empirical values of LDCs. The black dashed line is the line of equality between the x- and y- axis. On the other hand, the lower panel shows the distribution of residuals between the SPAM and empirical LDCs.

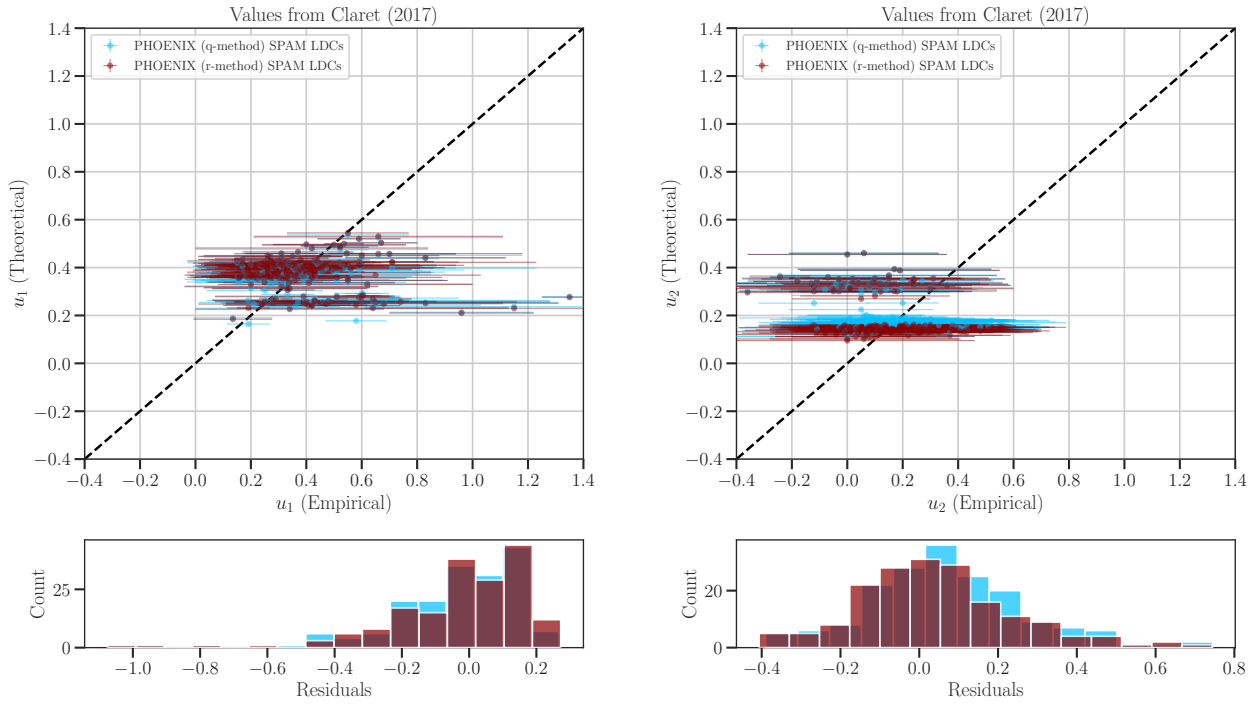


Figure 18. Comparison of the retrieved u_1 and u_2 coefficients from the TESS data with the SPAM LDCs which made use of tabulated values of non-linear LDCs from Claret (2017) using r -method and q -method.

For Tabular/Code LDCs

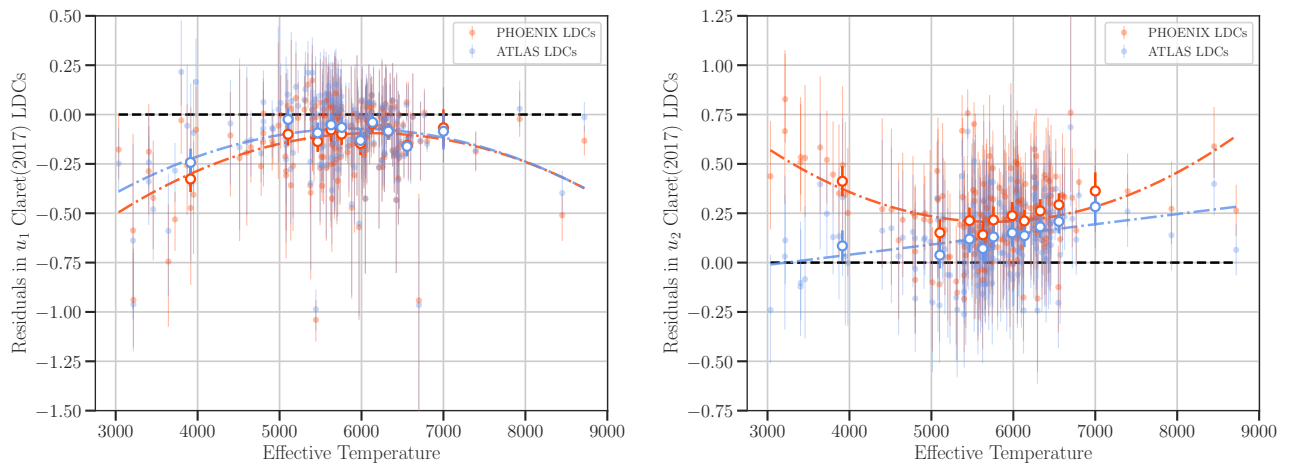


Figure 19. Temperature variation of offsets in u_1 and u_2 , when, theoretically, LDCs are calculated using LDCs provided by Claret (2017). The dashed-dotted lines show the best fitted model to the residuals.

For Tabular/Code LDCs

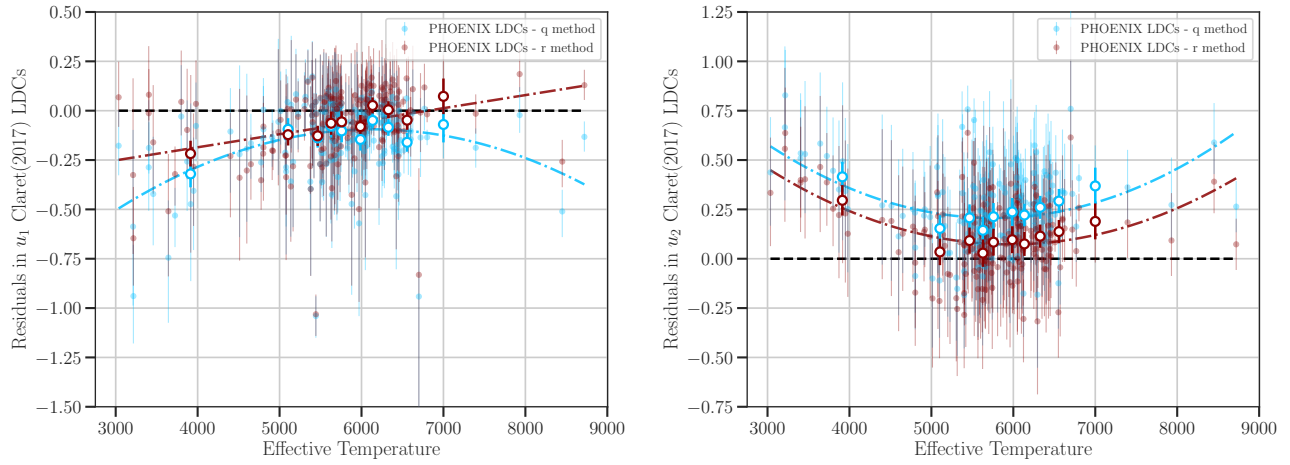


Figure 20. Temperature variation of offsets in u_1 and u_2 , when, theoretically, LDCs are calculated using tables provided by Claret (2017), using q -method and r -method. The dashed-dotted lines show the best fitted model to the residuals

For SPAM LDCs

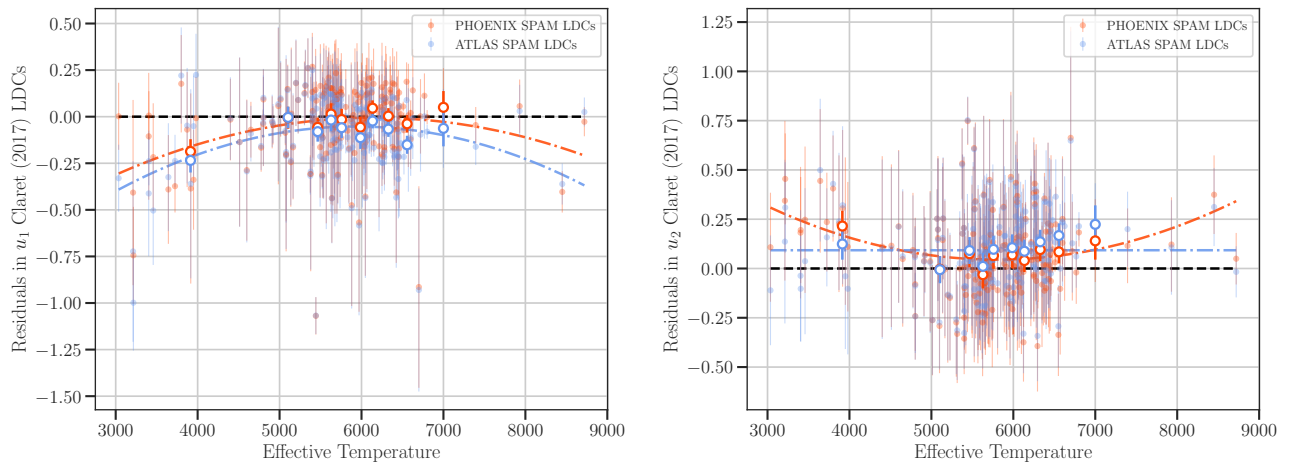


Figure 21. Same as Figure 19, but now using SPAM LDCs.

For SPAM LDCs

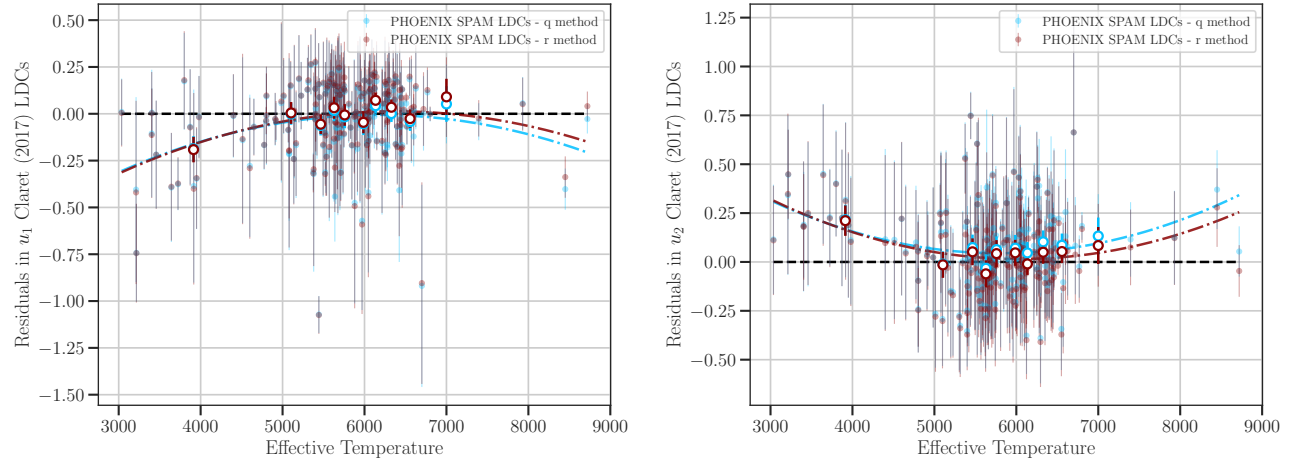


Figure 22. Same as Figure 20, but now using SPAM LDCs.